Asteroseismic modeling of gravity modes in slowly rotating A/F stars with radiative levitation

Joey S. G. Mombarg,[1] Aaron Dotter,[2] Timothy Van Reeth,[1] Andrew Tkachenko,[1] Sarah Gebruers,[1] and Conny Aerts[1, 3, 4]

[1]Institute of Astronomy, KU Leuven, Celestijnenlaan 200D, B-3001 Leuven, Belgium
[2]Center for Astrophysics | Harvard & Smithsonian, Cambridge, MA 02138, USA
[3]Department of Astrophysics, IMAPP, Radboud University Nijmegen, PO Box 9010, 6500 GL Nijmegen, The Netherlands
[4]Max Planck Institute for Astronomy, Koenigstuhl 17, 69117 Heidelberg, Germany

ABSTRACT

It has been known for several decades that transport of chemical elements is induced by the process of microscopic atomic diffusion. Yet, the effect of atomic diffusion, including radiative levitation, has hardly been studied in the context of gravity mode pulsations of core-hydrogen burning stars. In this paper, we study the difference in the properties of such modes for models with and without atomic diffusion. We perform asteroseismic modeling of two slowly rotating A- and F-type pulsators, KIC 11145123 ($f_{\rm rot} \approx 0.010$ d^{-1}) and KIC 9751996 ($f_{\rm rot} \approx 0.0696$ d^{-1}), respectively, based on the periods of individual gravity modes. For both stars, we find models whose g-mode periods are in very good agreement with the *Kepler* asteroseismic data, keeping in mind that the theoretical/numerical precision of present-day stellar evolution models is typically about two orders of magnitude lower than the measurement errors. Using the Akaike Information Criterion (AIC) we have made a comparison between our best models with and without diffusion, and found very strong evidence for signatures of atomic diffusion in the pulsations of KIC 11145123. In the case of KIC 9751996 the models with atomic diffusion are not able to explain the data as well as the models without it. Furthermore, we compare the observed surface abundances with those predicted by the best fitting models. The observed abundances are inconclusive for KIC 9751996, while those of KIC 11145123 from the literature can better be explained by a model with atomic diffusion.

Keywords: Asteroseismology, Stellar abundances, Stellar evolution, Stellar oscillations, Stellar processes, Stellar properties

1. INTRODUCTION

The mechanism(s) driving the transport of angular momentum (e.g. Aerts et al. 2019a) and chemical elements (e.g. Salaris & Cassisi 2017) within stars are still not understood from stellar evolution theory. Discrepancies between observations and theory have been shown for stars with birth masses between 1.3 and 8 M$_\odot$, which comprise a convective core, enshrouded by a radiative envelope (possibly with internal convective shells from partial ionization zones or a thin outer convective enve-

Corresponding author: Joey Mombarg
joey.mombarg@kuleuven.be

lope for $M_\star \lesssim 1.6$ M$_\odot$). In these radiative envelopes, the transport of chemical elements on a macroscopic scale is ascribed to convective core overshooting (e.g. Viallet et al. 2015), rotation (e.g. Maeder 2009), or internal gravity waves (IGW, e.g. Rogers & McElwaine 2017), whereas the transport of chemical elements on a microscopic scale is the result of atomic diffusion (Michaud et al. 2015). In stellar evolution codes, the description of macroscopic mixing introduces additional free parameters, whereas mixing from atomic diffusion can be derived from first principles. So far, the theory of element transport has been mainly evaluated by measurements of surface abundances. Asteroseismology constitutes a novel technique to empirically assess the conditions deep inside the interior of a star (Aerts et al. 2010), as well as

its evolutionary history (e.g. Bowman et al. 2019). The unprecedented high-quality data from the space-based *CoRoT* (Auvergne et al. 2009), *Kepler* (Borucki et al. 2010), and *TESS* (Ricker et al. 2015) missions allow for scrutiny of the current stellar evolution models of the stars' interiors by means of gravito-inertial asteroseismology (Aerts et al. 2018). The current state-of-the-art stellar models and pulsation codes are not capable of reproducing the observed oscillation frequencies of gravity (g) modes in γ Doradus (γ Dor, cf. Kurtz et al. (2014); Saio et al. (2015); Van Reeth et al. (2016); Schmid & Aerts (2016)) and Slowly-Pulsating B-type (SPB, cf. Pápics et al. (2014); Moravveji et al. (2015); Szewczuk & Daszyńska-Daszkiewicz (2018); Aerts et al. (2019b)) stars within the uncertainties of the data. Hence, additional physics is required in order to improve both the current stellar models as well as the prediction of the g-mode frequencies from these equilibrium models. Studies have already demonstrated the potential of g modes to distinguish between different near-core mixing profiles (Pedersen et al. 2018) and the temperature gradient close to the convective core interface (Michielsen et al. 2019). The work of Aerts et al. (2018) has evaluated a hierarchy of input physics when modeling g modes across a wide mass range. In the current work, we investigate to what extent the process of atomic diffusion can improve the theoretically predicted oscillation frequencies in two slowly rotating γ Dor stars.

Throughout this paper, we use the umbrella term 'atomic diffusion' to refer to the following four diffusion processes; *(i)* gravitational settling, *(ii)* thermal diffusion, *(iii)* concentration diffusion, and *(iv)* radiative levitation. The former process causes elements heavier than hydrogen to migrate towards the stellar center. This process of gravitational settling is counteracted by the process of radiative levitation where momentum is transferred from the radiative flux – generated in the core – to the atoms, thereby 'levitating' them outwards. The cross-section for photon absorption is larger for heavier elements and therefore radiative levitation will be most dominant on the heaviest elements, while the lighter elements will primarily be subjected to gravitational settling. Thermal diffusion works in the same direction as gravitational settling as heavier elements are pulled towards hotter regions due to the interaction with field protons (Michaud et al. 2015). The importance of atomic diffusion has already been pointed out in context of helioseismology (Christensen-Dalsgaard et al. 1993), chemical tagging (Dotter et al. 2017), and helium abundance determination (Verma et al. 2019, albeit without radiative levitation). Yet, when it comes to asteroseismic modeling of g-mode pulsators, this process is not

taken into account as it presents a computationally challenging task. Since g modes probe the stellar structure in the radiative region of stars where diffusive processes are at work, their frequencies will be dependent on the treatment of these processes in this region. The effect of atomic diffusion, especially radiative levitation, imposes implications on the determination of the properties of solar-like oscillators, as has been demonstrated by Deal et al. (2018, 2020). These authors focused their investigations on pressure (p) modes in solar-like oscillators, with masses up to $1.44\,M_\odot$. The dominant restoring force for p mode oscillations is the pressure force, whereas in this work we are concerned with gravito-inertial modes, for which the buoyancy and Coriolis force both act as restoring forces. For γ Dor stars, the mass regime is about $1.4\,M_\odot$ to $1.9\,M_\odot$ and thus covers a slightly higher mass regime where the force of the radiative levitation will be more dominant. Furthermore, the frequencies of g modes are dependent on the behavior of the chemical gradient in the near-core region. We aim to characterize the impact of atomic diffusion on the chemical gradient, and the implications for the g-mode frequencies.

Atomic diffusion might also be a key ingredient in the excitation of modes as it introduces accumulation of iron and nickel in the stellar layer where the opacity reaches its maximum (Richard et al. 2001; Deal et al. 2016; Hui-Bon-Hoa & Vauclair 2018), thereby altering the Rosseland mean opacity. This so-called 'opacity bump' occurs around a temperature of $200\,000\,\mathrm{K}$, i.e., the ionization temperature of iron. This may result in the forming of extra convection zones, which can excite pulsations through the κ-mechanism. Michaud et al. (2015) show these iron convection zones appear and disappear throughout the main-sequence lifetime for a 1.5-$M_\odot$ model, but are persistent for a 1.7-$M_\odot$ and a 1.9-$M_\odot$ model.

In this work we will focus our attention on the theoretically predicted adiabatic frequency values and compare them with those of observed modes. We take a data-driven approach and test our improved stellar models against observations from two stars observed by the nominal *Kepler* mission. As the effects of atomic diffusion might be (partially) washed out by rotationally induced mixing, we have selected two slowly rotating γ Dor stars for our purposes; KIC 11145123 and KIC 9751996. The former has been studied by Kurtz et al. (2014), who found 15 g-mode triplets ($m = 0$ modes with low visibility), one p-mode triplet, and one p-mode quintuplet. From the frequency splittings, a nearly uniform rotation period of $\sim100\,\mathrm{d}$ (upper limit of $f_{\mathrm{rot}} = 0.009512 \pm 0.000002$ d^{-1} from g modes) was

inferred. Such a slow rotation period is quite rare compared to observations from the study by Li et al. (2019b), who show that the rotation-period distribution – based on 611 γ Dor stars – is Gaussian-like and peaks around ∼1 d, although some excess around slow rotation is seen in the distribution. A spectroscopic follow-up of KIC 11145123 by Takada-Hidai et al. (2017) shows the star has a low surface metallicity ([Fe/H] = −0.71 ± 0.11 dex) and its low lithium abundance is compatible with those of the blue stragglers (Glaspey et al. 1994). Moreover, these authors did not find any presence of a companion. In this paper, we test whether the observed pulsation periods and surface abundances can be explained by a single star model with atomic diffusion taken into account. The second star, KIC 9751996, has a super-solar surface metallicity, [Fe/H] = +0.28 ± 0.07 dex (Van Reeth et al. 2015). Also for this star rotationally split modes were identified, yielding a rotation frequency of $0.0696 ± 0.0008\,\mathrm{d}^{-1}$ ($P_{\mathrm{rot}} = 14.4 ± 1.7\,\mathrm{d}$, Van Reeth et al. (2016)). KIC 9751996 is one of the 37 γ Dor stars in the sample analyzed by Momparg et al. (2019). In this work, we quantify the difference in inferred mass and age from asteroseismic modeling of the observed g-mode frequencies of both KIC 11145123 and KIC 9751996, using models with and without atomic diffusion.

2. METHODS

The accelerations due to radiative levitation in the stellar interior can be computed either by means of 'opacity sampling' (e.g. LeBlanc et al. 2000) or by using the Single-Valued Parameter (SVP) method (cf. Alecian & LeBlanc 2002; LeBlanc & Alecian 2004; Théado et al. 2012; Deal et al. 2020). In this work, we have used the opacity sampling method, which is a slightly more accurate method compared to the SVP method, but this increased accuracy comes at the cost of computation time. The inclusion of radiative levitation drastically increases the computation time of an evolution track, e.g., an increase by about a factor 100 (using four threads) when starting at the pre-main sequence (pre-MS) contraction up to the terminal age main-sequence (TAMS). Hence, we employ the method from Momparg et al. (2019) as a first estimate for the mass range of the grids to be constructed to model the individual periods from the effective temperature (T_{eff}), surface gravity ($\log g$), and the reduced asymptotic period spacing (Π_0). For the determination of Π_0 for KIC 9751996, we rely on the work by Van Reeth et al. (2016). Since the rotation period of KIC 11145123 is extremely long, we estimate Π_0 by taking the average period spacing of the central frequencies found by Kurtz et al. (2014) (0.0241 ± 0.0009 d), and use

Parameter	Lower boundary	Upper boundary	Step size
KIC 9751996			
$M_\star$	$1.65\,\mathrm{M}_\odot$	$1.90\,\mathrm{M}_\odot$	$0.01\,\mathrm{M}_\odot$
Z_{ini}	0.022	0.030	0.004
f_{ov}	$\in [0.0100, 0.0175, 0.0225, 0.0300]$		
f_{rot}	fixed at $0.0696\,\mathrm{d}^{-1}$		
KIC 11145123			
$M_\star$	$1.30\,\mathrm{M}_\odot$	$1.50\,\mathrm{M}_\odot$	$0.01\,\mathrm{M}_\odot$
Z_{ini}	0.002	0.004	0.001
f_{ov}	$\in [0.0100, 0.0175, 0.0225, 0.0300]$		
f_{rot}	fixed at $0.010\,\mathrm{d}^{-1}$		

Table 1. Extend of the grids used to model KIC 9751996 and KIC 11145123. Grids are computed for *(i)* standard OP opacities, without atomic diffusion, and *(ii)* OP monochromatic opacities with atomic diffusion.

$\Pi_0 \approx \Delta P_{\mathrm{co}} \sqrt{l(l+1)}$. The period spacing in the corotating frame ΔP_{co} is in this case roughly equal to the period spacing in the inertial frame. The coverages in metallicity for the two stars are based on spectroscopic measurements from Takada-Hidai et al. (2017) and Van Reeth et al. (2016) for KIC 11145123 and KIC 9751996, respectively, where the measured value and the upper and lower values of the uncertainty intervals listed in these studies are used. Besides the mass, the method by Momparg et al. (2019) also provides us with an estimate for the hydrogen mass fraction inside the convective core (X_{c}). These estimates indicate both stars have $X_{\mathrm{c}} \lesssim 0.3$. Following Fig. 8 of Deal et al. (2018), the measured [Fe/H] should not differ more than 0.1 dex from the initial value. Therefore, the observed iron surface abundance will most likely be a good approximation of the star's initial bulk metallicity, Z_{ini}. Nevertheless, we have also tested if the pulsations can be explained by models with atomic diffusion at solar metallicity. Table 1 summarizes the extent of the grids used in this work (the grid where Z_{ini} is fixed at 0.014 covers the same ranges for the other input parameters).

2.1. Stellar models

The stellar models were computed using the stellar evolution code MESA (Paxton et al. 2011, 2013, 2015, 2018, 2019), r11701. For both the grid with and without atomic diffusion the opacities from the Opacity Project (OP; Seaton (2005)) were used, where we relied on the monochromatic opacities for the computations of the accelerations due to radiative levitation. The Rosseland mean opacity is computed from the monochromatic opacities for models with atomic diffusion. We point out that the computation time of models using the OP monochromatic opacity tables has been improved com-

pared to MESA revisions released prior to MESA Paper V (Paxton et al. 2019), and these models also benefit from multi-treading. A solar mixture according to Asplund et al. (2009) is assumed, as spectroscopic studies of γ Dor stars have shown that these stars have abundance patterns similar to that of the Sun (e.g. Kahraman Aliçavuş et al. 2016). From this mixture the metal abundances are scaled with Z_{ini}.

The boundary of the convective core is defined according to the Ledoux criterion and we impose diffusive convective core overshooting. The core boundary mixing (CBM) efficiency, D_{CBM}, is then parameterized as per Freytag et al. (1996) by

$$D_{\mathrm{CBM}}(r) = D_{\mathrm{CBM}}(r_0) \exp\left(\frac{-2(r - r_0)}{f_{\mathrm{ov}} H_{\mathrm{P}}(r_{\mathrm{cb}})}\right), \quad (1)$$

where $D_{\mathrm{CBM}}(r_0)$ is the mixing coefficient at the starting point of the overshoot profile, and $H_{\mathrm{P}}(r_{\mathrm{cb}})$ the pressure scale height at the convective boundary radius r_{cb}. The starting point of the overshoot profile r_0 is placed at a radius $r_{\mathrm{cb}} - f_0 H_{\mathrm{P}}(r_{\mathrm{cb}})$, since $D_{\mathrm{CBM}}(r)$ drops off steeply at the core boundary, making it non-trivial to define its value precisely at r_{cb}. In this work, we adopted a value $f_0 = 0.005$. The mixing at the boundary of convective shells and at the bottom of the surface convection zone is described by the same formalism presented in Eq. (1), for which we set $f_{\mathrm{ov}} = 0.015$. The basic chemical reaction network in MESA is extended to include Ne, Na, Al, Si, S, Ca, Fe, and Ni. We considered two ways to set the initial chemical composition $(X_{\mathrm{ini}}, Y_{\mathrm{ini}}, Z_{\mathrm{ini}})$. In a first approach, we fix the initial hydrogen content $X_{\mathrm{ini}} = 0.7154$ and leave the initial metallicity Z_{ini} as a free parameter, following the larger importance of estimating Z_{ini} compared to Y_{ini} for g-mode asteroseismology of intermediate-mass stars (Moravveji et al. 2015). The initial helium content is then set by $Y_{\mathrm{ini}} = 1 - X_{\mathrm{ini}} - Z_{\mathrm{ini}}$ once Z_{ini} is chosen. The ^{2}H/^{1}H and ^{3}He/^{4}He isotope ratios are set to $2 \cdot 10^{-5}$ and $1.66 \cdot 10^{-4}$, respectively, as per Asplund et al. (2009). We have chosen this approach to set the initial composition as Takada-Hidai et al. (2017) have estimated asteroseismically that KIC 11145123 has a high initial helium abundance ($Y_{\mathrm{ini}} = 0.297$), compared to the chemical enrichment rate $Y_{\mathrm{ini}} = 0.244 + 1.226 Z_{\mathrm{ini}}$ found by Verma et al. (2019). In a second approach, we use this enrichment rate by Verma et al. (2019), despite its large uncertainties, to set the initial composition for both stars. The initial composition of the models presented in this section and in Sec. 3 is set by fixing X_{ini}. As atmospheric boundary condition, an Eddington gray atmosphere is used, for which the solar-calibrated mixing length parameter $\alpha_{\mathrm{MLT}} = 1.713$ (Choi et al. 2018). This value of

α_{MLT} has been calibrated with models including atomic diffusion. Omitting atomic diffusion in the stellar evolution models will affect the inferred value of this parameter. The impact of α_{MLT} on the reduced asymptotic period spacing, Π_0, has been assessed by Johnston et al. (2019b) and Mombarg et al. (2019). Both these studies show α_{MLT} to have a small effect on Π_0, compared to typical uncertainties for this quantity derived from the *Kepler* photometry by Van Reeth et al. (2016). Furthermore, a small amount of additional mixing is imposed in the radiative zone. A constant mixing efficiency of $D_{\mathrm{mix}}(r) = 1.0 \; \mathrm{cm}^2\,\mathrm{s}^{-1}$ is chosen, following the asteroseismic study by Van Reeth et al. (2016). At the start of each model, a pre-MS model is computed with atomic diffusion already turned on, such that a consistent comparison can be made. No diffusion computations are done in convective zones where the material is assumed to be instantaneously mixed.

2.2. Computations of radiative levitations

Radiative levitations are computed for the elements ^{1}H, ^{3}He, ^{4}He, ^{12}C, ^{14}N, ^{16}O, ^{20}Ne, ^{23}Na, ^{24}Mg, ^{27}Al, ^{28}Si, ^{32}S, ^{40}Ca, ^{56}Fe, and ^{58}Ni. The description of atomic diffusion in MESA is based on Burgers' equations (Burgers 1969), following the routines by Thoul et al. (1994) for settling and temperature/concentration gradients,

$$\frac{p}{K_0}\left(\alpha_i \frac{d\ln p}{dr} + \nu_i \frac{d\ln T}{dr} + \sum_{j=1, \neq e}^{S} \gamma_{ij} \frac{d\ln C_j}{dr}\right)$$
$$= \sum_{j=1}^{2S+2} \Delta_{ij} W_j, \quad (2)$$

that solve for W_j, describing the mean diffusion velocity of species j, where p is the pressure, T the temperature, and C_j the concentration of species j. The latter is defined as,

$$C_j = n_j/n_e, \quad (3)$$

with n_j and n_e the number densities of the species and electrons, respectively. The sum is taken over all S species (that includes electrons as well) and W_j is defined as follows,

$$W_j = \begin{cases} w_j & \text{for } j \in [1, S] \\ r_j & \text{for } j \in [S+1, 2S] \\ K_0^{-1} n_e e E & \text{for } j = 2S+1, \\ K_0^{-1} n_e m_{\mathrm{p}} g & \text{for } j = 2S+2, \end{cases}$$

where w_j is the mean diffusion velocity and r_j the residual heat flow velocity of a species. We refer to Thoul

et al. (1994) for the extensive details, as well as the definition of the constants K_0, α_i, ν_i, γ_{ij} and Δ_{ij}. MESA uses the diffusion coefficients from Stanton & Murillo (2016) for the ion-ion terms and the coefficients from Paquette et al. (1986) for electron-ion terms to compute the Δ_{ij} coefficients. The inclusion of radiative levitation in MESA has been incorporated following Hu et al. (2011), along with some modifications for which we refer to the MESA Paper III (Paxton et al. 2015). When accelerations induced by radiative levitation, $g_{\mathrm{rad},i}$, are included, Eq. (2) becomes

$$\frac{p}{K_0}\left(-\frac{\alpha_i m_i g_{\mathrm{rad},i}}{k_B T} + \alpha_i \frac{d\ln p}{dr} + \nu_i \frac{d\ln T}{dr}\right.$$
$$\left. + \sum_{j=1,\neq e}^{S} \gamma_{ij}\frac{d\ln C_j}{dr}\right) = \sum_{j=1}^{2S+2}\Delta_{ij}W_j, \quad (4)$$

where m_i is the mass of species i. The acceleration induced by radiative levitation according to Hu et al. (2011) is computed as

$$g_{\mathrm{rad},i} = \frac{\mu \kappa_{\mathrm{R}}}{\mu_i c}\frac{l(r)}{4\pi r^2}\int_0^\infty \frac{\sigma_i(u)[1-e^{-u}] - a_i(u)}{\sum_k f_k \sigma_k(u)}\mathrm{d}u, \quad (5)$$

where μ is the mean molecular weight, μ_i the molecular weight of species i, c is the speed of light, $l(r)$ the luminosity at radius r and κ_{R} the Rossland mean opacity. The integral is taken over $u = h\nu/k_B T$ (h en k_B the Planck and Boltzmann constant, respectively), with $\sigma_i(u)$ the monochromatic opacity cross-section for absorption and scattering, $a_i(u)$ a correction term, and f_i the so-called 'number fraction' such that the sum over all species yields the total cross-section of the mixture. In Fig. 1 we show the profiles of the mixing efficiency and the opacity (top panel) as well as the (fully ionized) mean molecular weight $\mu \approx 1/(2X + 3/4Y + Z/2)$ and $\nabla_\mu = \mathrm{d}\ln\mu/\mathrm{d}\ln p$ (bottom panel) for a 1.7-$\mathrm{M}_\odot$ star. To ensure numerical stability, the outer $10^{-5}\%$ of the mass is treated as a single cell for the purposes of atomic diffusion. This explains why the helium convection zone (around $\log T = 4.6$) is still present in Fig. 1, as gravitational settling of helium would otherwise increase the local μ, since $g_{\mathrm{rad,He}} \ll g$, thereby stabilizing this convection zone. However, the probing power of g modes is weak at the stellar surface, compared to the near-core region, and hence, such a numerical approximation has a negligible effect on the asteroseismic modeling performed in this paper. We do point out Deal et al. (2016) observe an iron convection zone around $\log T = 5.3$ for stars $M_\star \gtrsim 1.7\mathrm{M}_\odot$. Here, we only observe such a convection zone when the opacities are artificially increased with a factor 5 around the Z-bump, in agreement with the study by Guzik et al. (2018). It
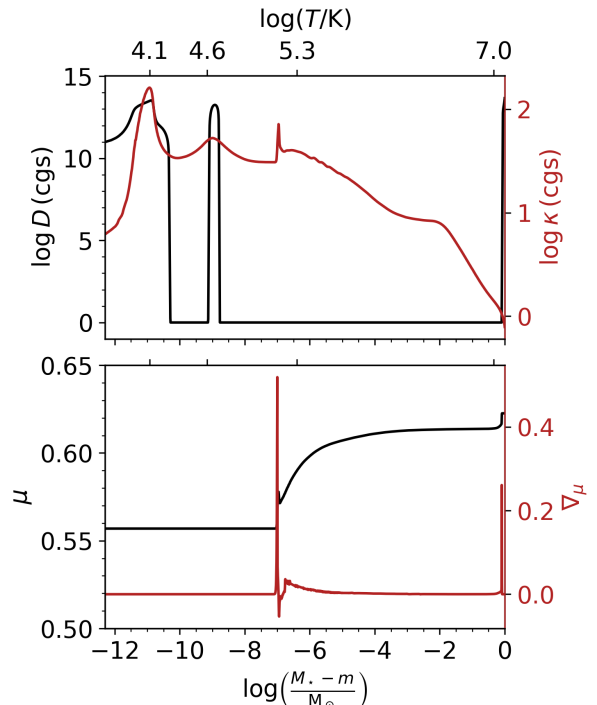

Figure 1. *Top panel:* Profiles of the mixing efficiency (in black) and Rossland mean opacity (in red) for a 1.7-$\mathrm{M}_\odot$ model ($Z_{\mathrm{ini}} = 0.014$, $f_{\mathrm{ov}} = 0.0225$) with an age of 100 Myr, when atomic diffusion is active. *Bottom panel:* Corresponding profile of the mean molecular weight (fully ionized) μ, and ∇_μ.

is not surprising that differences between model properties in the outer envelope resulting from different codes occur, as the computations by Deal et al. (2016) rely on the SVP approximation while we used the opacity sampling method and treated the $10^{-5}\%$ of outer mass as a single cell for atomic diffusion. Such differences in the properties of the outer envelope are not important for g-mode asteroseismology, because the kernels of such modes probe the deep interior layers of the stars and not the outer envelope.

2.3. Pulsation computations

For each stellar model in the grids, the theoretical pulsation frequencies are computed in the adiabatic approximation using the stellar pulsation code GYRE (Townsend & Teitler 2013; Townsend et al. 2018), version 5.2. For both KIC 11145123 and KIC 9751996, dipole modes have been observed. For both stars, we fix the rotation frequency to the measured value (cf. Table 1), as the near-core rotation rates have been precisely determined in a model-independent way from mode splitting. As both stars are slow rotators – rotation frequency much smaller than 10% of the Roche critical rotation – it is

justified to use the traditional approximation of rotation
(TAR, Eckart (1960)) to compute the frequencies of the
g modes. Here, the effect of only the (local) vertical
component of the Coriolis force is taken into account (cf.
Ouazzani et al. 2019). Li et al. (2019a) have shown that
the typical range of excited radial orders for γ Dor stars
spans from about -20 to -100. Yet, we limit the com-
putations to a radial order range between $n = -15$ and
$n = -45$, based on the identified orders by Kurtz et al.
(2014) and Van Reeth et al. (2016), for KIC 11145123
and KIC 9751996, respectively.

3. THE EFFECT OF ATOMIC DIFFUSION

Within the mass regime covered by γ Dor stars, the
forces on the chemical elements due to gravity and radia-
tive levitation are competing with each other (Turcotte
et al. 1998; Deal et al. 2020). In Fig. 2, we show the
$g_{\mathrm{rad},i}$ for a few heavy elements, compared to the grav-
itational acceleration in a 1.7-$M_\odot$ star. We see that
it is important that both these diffusion processes are
taken into account for this mass regime, as only in-
cluding gravitational settling yields unphysical surface
abundances (Morel & Thévenin 2002). However, the
counteracting role of radiative levitation may also be
(partly) taken up by additional mixing processes such as
turbulent diffusion (e.g. Dotter et al. 2017), rotational
mixing (e.g. Deal et al. 2020) or IGW. For the elements
plotted in Fig. 2, we report that the order of magni-
tude and global behavior of $g_{\mathrm{rad},i}$ in our MESA model
is in agreement with the 1.7-$M_\odot$ model computed with
the Montreal/Montpellier code by Richard et al. (2001).
Contrary to MESA, the Montreal/Montpellier code uses
the monochromatic opacities from the OPAL project.

The settling of heavier elements, mainly helium, has
a stabilizing effect on the chemical gradient (Théado
et al. 2009) that results from a receding core as the
local mean molecular weight is increased. Hence, the
profile of the Brunt-Väisälä frequency is altered in the
region where g modes are most sensitive. In Fig. 3 the
effect of diffusion on the chemical gradient (∇_μ) and on
the Brunt-Väisälä frequency (N) is demonstrated. The
migration of the chemical elements for which radiative
levitation is computed is shown in Fig. 4 for three differ-
ent moments throughout the main-sequence evolution.
Similar behavior is seen when we compare the behavior
of the accumulation of the chemical elements shown in
Fig. 4 to that found by Deal et al. (2018) (their Fig. 1,
similar metallicity of $Z = 0.025$). The absence of a
decrease in X_i at the bottom of the surface convection
zone for Fe and Al is the result of a different treatment
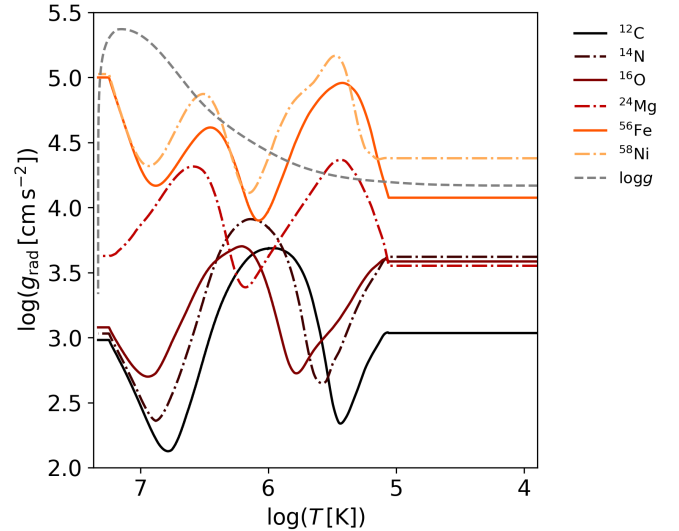of overshooting at the boundaries of internal convective

Figure 2. Accelerations induced by radiative levitation of
several heavy elements in a 1.7-$M_\odot$ star at $X_c = 0.50$ (Z_{ini}
$= 0.014$, $f_{\mathrm{ov}} = 0.0175$). The gravitational acceleration is
indicated by the dashed gray line. For numerical purposes
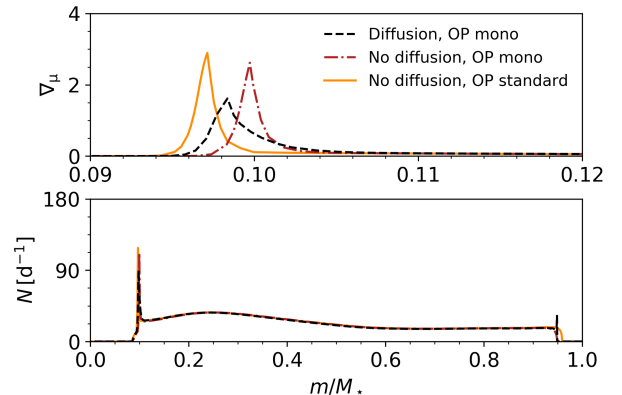$g_{\mathrm{rad},i}$ is kept constant in the outermost cells.

Figure 3. The effect of atomic diffusion on the chemical gra-
dient (top panel) and the Brunt-Väisälä frequency (bottom
panel) in a 1.4-$M_\odot$ star around $X_c = 0.6$ with solar metal-
licity ($Z_{\mathrm{ini}} = 0.014$). A comparison is shown for a model
computed with the standard OP tables and one using the
monochromatic OP opacities.

shells and the bottom of the thin outer convective enve-
lope.

Gravity-mode frequency shifts are the net result of the
use of a different opacity source, and the changes in the
chemical stratification introduced by atomic diffusion.
Fig. 5 shows the frequency differences between a model
with atomic diffusion (OP monochromatic opacities),
and two models without atomic diffusion, one with the
OP monochromatic opacities, and one with the standard
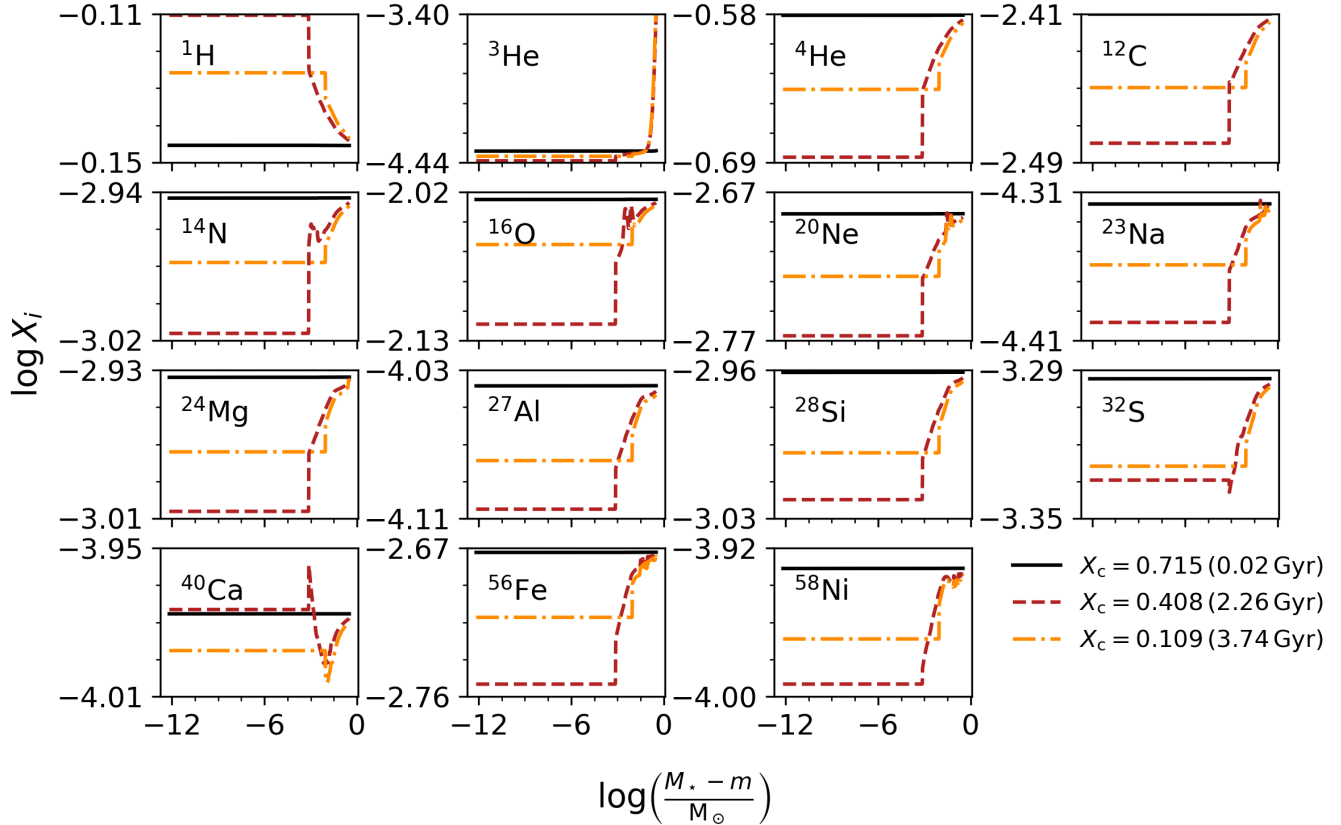OP tables. The changes in input physics are mostly felt

Figure 4. Evolution of the mass fractions throughout a 1.4-$M_\odot$ star with $Z_{\mathrm{ini}} = 0.022$ and $f_{\mathrm{ov}} = 0.0175$ when atomic diffusion is active. The quantity m indicates the mass enclosed within a sphere of radius r, hence the distance to the stellar center decreases when moving to the right along the abscissa.

by the lower radial orders, as can be seen in Fig. 5. It should be noted that larger frequency differences occur for metallicities deviating from solar metallicity as a result of the uncertainties on the monochromatic opacity tables. As can be seen from Fig. 5 the frequency shifts caused by atomic diffusion alone (orange points) are in any case larger than the Rayleigh limit of a 1-year long lightcurve. The frequency difference as a function of radial order seems to follow a trend, as the models without diffusion tend to either over- or underestimate the frequencies calculated from the models with diffusion. However, parametrizing a correction on the frequencies predicted by a model without atomic diffusion to obtain the predicted frequencies by a model with atomic diffusion is non-trivial as the frequency difference per radial order is dependent on the mass, age, and composition of the star, as is shown in Fig. 5 for the latter two parameters.

4. ASTEROSEISMIC MODELING

To date, the modeling of g modes in single γ Dor stars, relied on Π_0 as asteroseismic input, combined with the

T_{eff} and $\log g$ from spectroscopy (Mombarg et al. 2019). In this work, we investigate if replacing the asteroseismic input with the periods of the individual pulsations, instead of Π_0, will improve upon the constraining of the mass and age, as this has never been studied for A/F-type g-mode pulsators. Commonly, the pulsations are presented in a so-called period spacing pattern, where the spacing between two periods of consecutive radial orders ($\Delta P = P_{n+1} - P_n$) is plotted as a function of P_n, which we have illustrated for KIC 9751996 and KIC 11145123 in Fig. 6. The spectroscopic measurements have relatively larger uncertainties with respect to those for the periods of the g modes (see Table 1 in Aerts et al. 2019a), and there are only two spectroscopic input parameters compared to about 30 periods for each of the two stars. Therefore, adding T_{eff} and $\log g$ will not contribute much to the goodness of fit, as we demonstrate in Sections 4.1 and 4.2. In addition, we also only fit the pulsations and use the spectroscopic measurements a posteriori to eliminate models that do not agree with the measured T_{eff} and $\log g$ within the 1σ uncertainties. Selection of the best model is done by fitting each of the observed identified periods of the
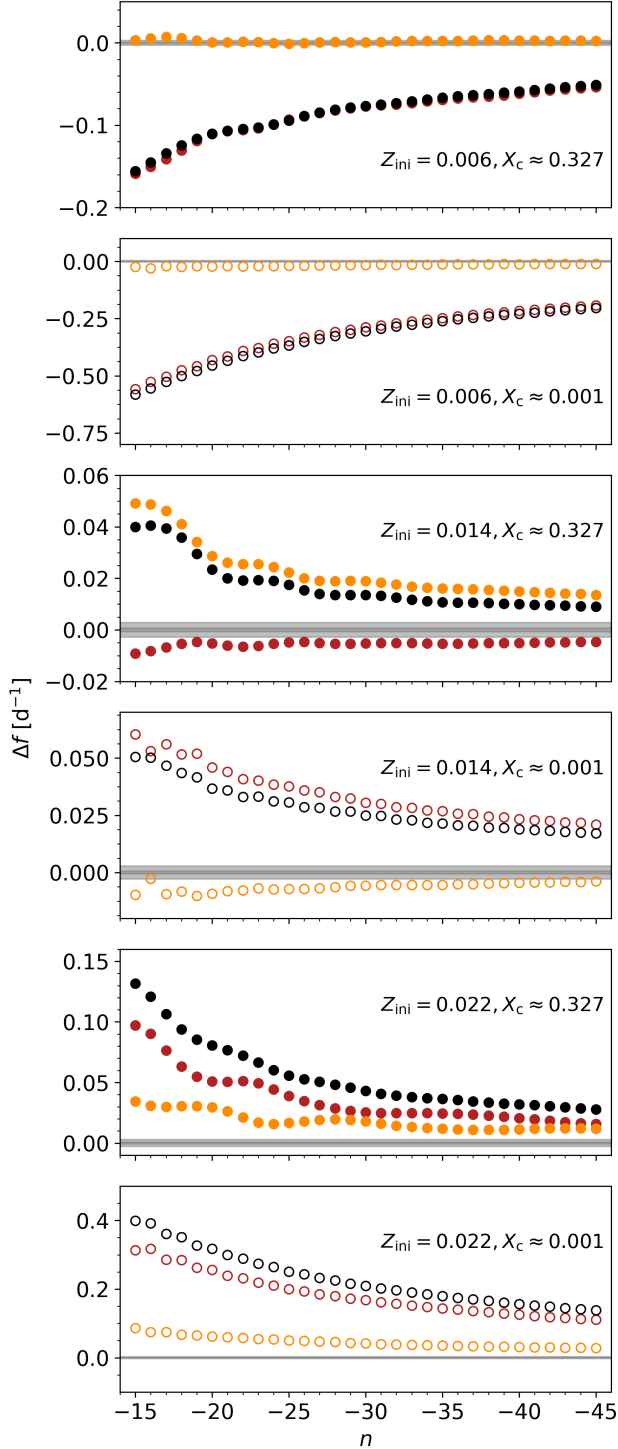
g modes for each azimuthal order. Starting with the longest period spacing sequence (see Fig. 6), the lowest observed period, P_1^{obs}, is assigned to the closest period of the theoretical model and the consecutive observed periods are then assigned to the consecutive radial orders. The radial order identification is then repeated for the next longest sequence (if present), demanding a radial order cannot be assigned multiple times. If this is the case, the model is removed from consideration.
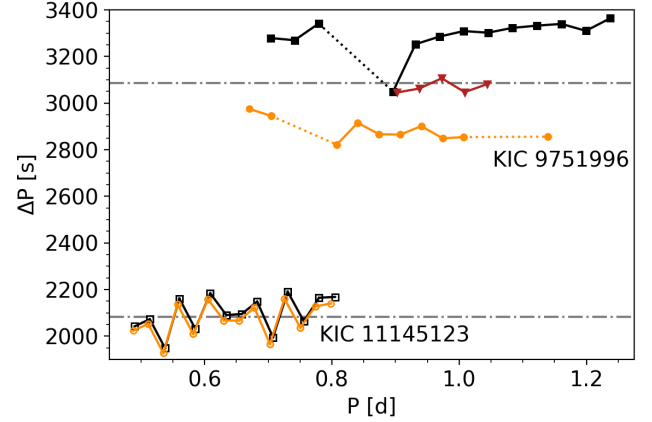
Figure 6. Period spacing patterns of KIC 9751996 (Van Reeth et al. 2016) and KIC 11145123 (Kurtz et al. 2014). The fitting is done as follows. For each azimuthal order (black squares: $m = -1$, maroon triangles: $m = 0$, orange circles: $m = 1$), the smallest period of each continuous sequence is assigned to a theoretical mode period and the consecutive periods to consecutive radial orders, starting with the longest sequence. The continuous sequences are separated by dotted lines. The gray lines indicate the measured values of $\Pi_0/\sqrt{\ell(\ell+1)}$, where $\ell = 1$.

Aerts et al. (2018) describe the Mahalanobis distance as a merit function to account for the variance of the individual mode periods across a grid of stellar models to take into account correlations between and heteroscedasticity of the measured g-mode periods and the stellar parameters to be estimated. This merit function has already been applied to asteroseismic modeling using (Π_0, T_{eff}, $\log g$) by Johnston et al. (2019b) and Mombarg et al. (2019), and using photometric colors in the context of clusters by Johnston et al. (2019a), but has never been applied to individual pulsations in γ Dor stars. However, in this study we work with grids covering relatively small ranges for computational reasons and these do not allow to assess the variance-covariance matrix for the theoretically predicted pulsation periods in an adequate way. For this reason, we use the simplified version of the Mahalanobis distance, which ignores the variance-covariance structure among the observed mode periods. This simplified version corresponds with

Figure 5. Difference in frequency ($\Delta f = f_{n,1} - f_{n,2}$, where model 2 is the baseline without diffusion) for a 1.4-$M_\odot$ model ($f_{\mathrm{ov}} = 0.0175$) as a function of radial order n. *Black symbols:* baseline with standard OP tables. *Orange symbols:* baseline with OP monochromatic opacities. *Maroon symbols:* both without diffusion, but different opacity sources. The light and dark shaded areas mark the Rayleigh limit ($1/T$) for a 351-day (*TESS* CVZ) and a 4-year timebase (*Kepler* nominal mission), respectively. Rotation is not taken into account in the pulsation computations of this illustration.

the reduced χ^2, defined as,

$$\chi^2_{\mathrm{red}} = \frac{1}{N-k} \sum_i^N \frac{\left(P_i^{(\mathrm{th})} - P_i^{(\mathrm{obs})}\right)^2}{\sigma_{P_i}^2}, \qquad (6)$$

where N is the number of observed g-mode periods and k the number of free parameters.

In addition to the pulsations, the fingerprints of atomic diffusion are also revealed at the stellar surface, as the process alters the surface abundances during the evolution of the star. Since the migration of each chemical species is different, from the chemical surface composition, one might be able to determine whether atomic diffusion is indeed active in a star, assuming an age and initial composition. For the models that best reproduce the observed periods and spectroscopic measurements, a comparison is made between the predicted and observed surface abundances, as an additional test for the influence of atomic diffusion. We stress that the surface abundances are not fitted, as both the observational and theoretical values have large uncertainties.

Besides the surface abundances being altered by atomic diffusion, it might also be possible that the star was born with a solar metallicity, but its metal abundances at the surface have been altered as a result of atomic diffusion. Hence, both stars are also fitted to grids where we fix $Z_{\mathrm{ini}} = 0.014$ (same mass and overshoot ranges compared to the grids with the metallicity set according to the spectroscopic value). Since for solar metallicity the difference between the two discussed options of setting Y_{ini} is negligible, we only explore the option where X_{ini} is fixed for this case. The observed periods of both stars are fitted to the grids described in Table 1, where we have used the OP monochromatic opacities for the diffusion models and the OP tables (non monochromatic) from `MESA` for the models without diffusion. In order to make a meaningful comparison between the models with and without atomic diffusion, the Akaike Information Criterion (AIC) is evaluated. We use the AIC, corrected for a small sample size, defined as follows,

$$\mathrm{AIC} = \chi^2 + \frac{2kN}{N-k-1}, \qquad (7)$$

where N is number of observed periods, and k the number of free parameters. The grid with fixed metallicity has one degree of freedom less, while k does not change when diffusion is taken into account. When comparing two models A and B, model B is favored over model A if $\Delta\mathrm{AIC} = \mathrm{AIC}_A - \mathrm{AIC}_B > 2$, where the evidence is (very) strong if $\Delta\mathrm{AIC} > 6$ (10) (Kass & Raftery 1995). These regimes stem from the value of $2\ln[P(D|\mathrm{A})/P(D|\mathrm{B})]$, where $P(D|\mathrm{X})$ is the probability of the observations D

given model X. For example, a difference $\Delta\mathrm{AIC} = 6$ means the probability of producing the data with model A is roughly 95%.

4.1. Models without atomic diffusion

We first fit both stars to the respective grids without atomic diffusion listed in Table 1 to test if an adequate solution can be found, when the individual mode periods are used as input, instead of Π_0 as was done in Mombarg et al. (2019).

4.1.1. KIC 9751996

When using T_{eff} and $\log g$ from spectroscopy as additional input, along with the g-mode periods, we find a best model with the parameters listed in Table 5 in Appendix A (only for fixed X_{ini}). Given the observed values of T_{eff} and $\log g$ (Table 3) and their respective uncertainties, the acquired model is consistent within 2σ. When we demand the model which best fits the pulsations is consistent within the 1-σ uncertainty intervals of these two spectroscopic observables, the model M01 listed in the first column of Table 2 is found. The choice of the initial composition impacts the obtained stellar parameters (see Table 2). This is expected as the predicted mode periods are degenerate with respect to mass and metal fraction, i.e. decreasing the mass of a model has the same effect on the mode periods as increasing the metal fraction (Moravveji et al. 2015, 2016; Mombarg et al. 2019). Similarly, increasing the metal fraction shifts T_{eff} to cooler temperatures. Therefore, imposing a cutoff in T_{eff} will yield more massive models. Mombarg et al. (2019) estimated the mass of KIC 9751996 to be $1.95 \pm 0.10\,M_\odot$, situated on the MS around $X_c/X_{\mathrm{ini}} = 0.20^{+0.10}_{-0.12}$ (where $X_{\mathrm{ini}} = 0.71$), assuming the same $D_{\mathrm{CBM}}(r)$ description as in Eq. (1). However, that study assumed a metallicity close to the solar value. Indeed, when the observed [M/H] is assumed to be representative of the initial metallicity, a lower mass is found, as is expected from the well-known degeneracy between mass and metallicity for the predicted pulsation frequencies.

As can be seen from the χ^2 distributions in Fig. 7, modeling the individual pulsation periods does not allow us to constrain the mass further in comparison to using $(\Pi_0, T_{\mathrm{eff}}, \log g)$ as input. For the two ways of setting the initial composition as discussed in Sec. 2, we acquire a best solution. The solution with the lowest χ^2_{red} out of these two is presented in Table 1 and the other solution is presented in Appendix A. Setting the initial composition as per Verma et al. (2019), does yield a slightly better fit compared to fixing X_{ini} (model M01; shown in gray in Fig. 8). We find that the estimated values for $M_\star$ and X_c are consistent with the values from Mombarg
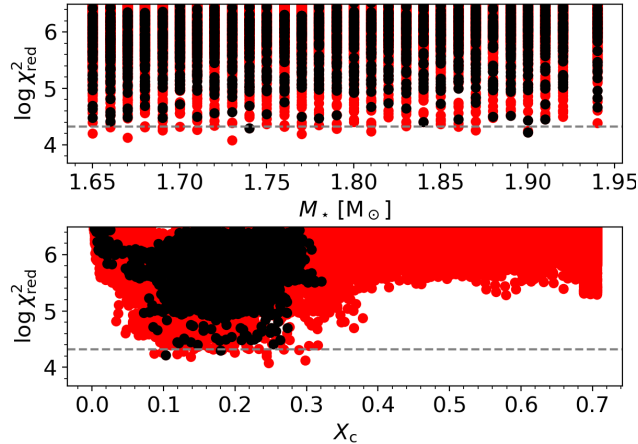
Figure 7. Reduced χ^2 distributions when modeling KIC 9751996 with the grid without diffusion where Y_{ini} is set as per Verma et al. (2019). The red dots indicate the models which have been eliminated since these do not agree with the 1-σ uncertainties on T_{eff} and $\log g$. The dashed gray line indicates the 1-σ confidence interval for the black dots.

et al. (2019). The corresponding predicted periods of the best-fitting model after a 1-σ cutoff in T_{eff} and $\log g$ are shown in the middle row of each panel in Fig. 8 (red/gray triangles; model M02/M01) and the evolution track is shown in Fig. 9. The uncertainties of g-mode predictions from evolutionary models and pulsation computations are typically of order $10^{-3}\,\mathrm{d}^{-1}$, which is two to three orders of magnitude above the uncertainties of observed modes from the nominal *Kepler* mission (cf. Aerts et al. 2018). Hence, we are dealing with large χ^2 as is well known from the modeling of g modes (e.g. Moravveji et al. 2016).

4.1.2. *KIC 11145123*

Including T_{eff} and $\log g$ in the fit yields the best-fitting model listed in the first column of Table 6 in Appendix A. In this case, the predicted T_{eff} and $\log g$ are in disagreement with the observed values, and adding these two input parameters compared to 30 periods does not remedy this inconsistency. Moreover, the obtained mass is at the edge of the grid, below which we deem it is unlikely for a star to show g-mode pulsations. Eliminating models in disagreement with the spectroscopic values of T_{eff} and $\log g$ instead forces the best solution to the higher edge of the mass coverage. Therefore, we have expanded the grids without atomic diffusion from $1.5\,\mathrm{M}_\odot$ to $1.7\,\mathrm{M}_\odot$ (cf. Fig. 10).

KIC 11145123 is most likely, judging from the value of Π_0 and the low rotation rate, near the end of hydrogen-core burning, as is found by Kurtz et al. (2014), who did not have any spectroscopic measurements for the star at

the time of their asteroseismic interpretation. However, the measured $\log g = 4.22\pm0.13$ from Takada-Hidai et al. (2017) would suggest the star is in the earlier phase of the MS. Therefore, we relax the demand on $\log g$ and allow it to be within 3σ instead, yielding the model listed in Table 2 (see Table 6 in the appendix for the 1-σ cutoff solution). In case of KIC 11145123, we are not able to fit the observed mode periods as well as for KIC 9751996 when atomic diffusion is not taken into account as is shown in Fig. 11 (triangles). The evolution track of the best-fitting model (M06) is shown in Fig. 12. We find that when a higher Y_{ini} is assumed, the observed mode periods are better matched, compared to when Y_{ini} is set to the predicted value according to the enrichment rate by Verma et al. (2019) (models M07 and M09; gray symbols in Fig. 11).

4.2. *Models with atomic diffusion*

We now fit both stars to the respective grids with atomic diffusion included (same parameter ranges) to test if the theoretical predictions yield a better match with the observations. As mentioned before, when atomic diffusion is included, the measured metallicity at the surface may not be representative of the initial metallicity. Therefore, we also fit both stars to grids where we fix the initial metallicity, $Z_{\mathrm{ini}} = 0.014$.

4.2.1. *KIC 9751996*

For the grids with atomic diffusion, we also explored both methods of including the spectroscopic parameters in the fit or using these parameters as a posteriori elimination criterion. The results of the primer method are presented in Table 5 in Appendix A, for which we again find that adding T_{eff} and $\log g$ does not enforce solutions consistent with spectroscopy. Table 2 summarizes the best-fitting models when we apply the 1σ cutoff in T_{eff} and $\log g$. The corresponding χ^2 distributions are shown in Figs 13 and 14. When the metallicity is taken according to the spectroscopically determined value, we find a higher mass compared to the solution where atomic diffusion is not included. The mass-metallicity relation is still seen in the solutions when T_{eff} and $\log g$ are also fitted (for fixing X_{ini} only), but this improves when we eliminate the models inconsistent with the measured spectroscopy. All grids with atomic diffusion included give X_{c} estimates (models M03, M04, M05) which are higher than the estimated value by Mombarg et al. (2019). The determined $\Pi_0 = 4364 \pm 7\,\mathrm{s}$ of KIC 9751996 by Van Reeth et al. (2015) cannot be reproduced by any of the best models, with or without atomic diffusion, and regardless whether T_{eff} and $\log g$ are fitted or used as a cutoff.
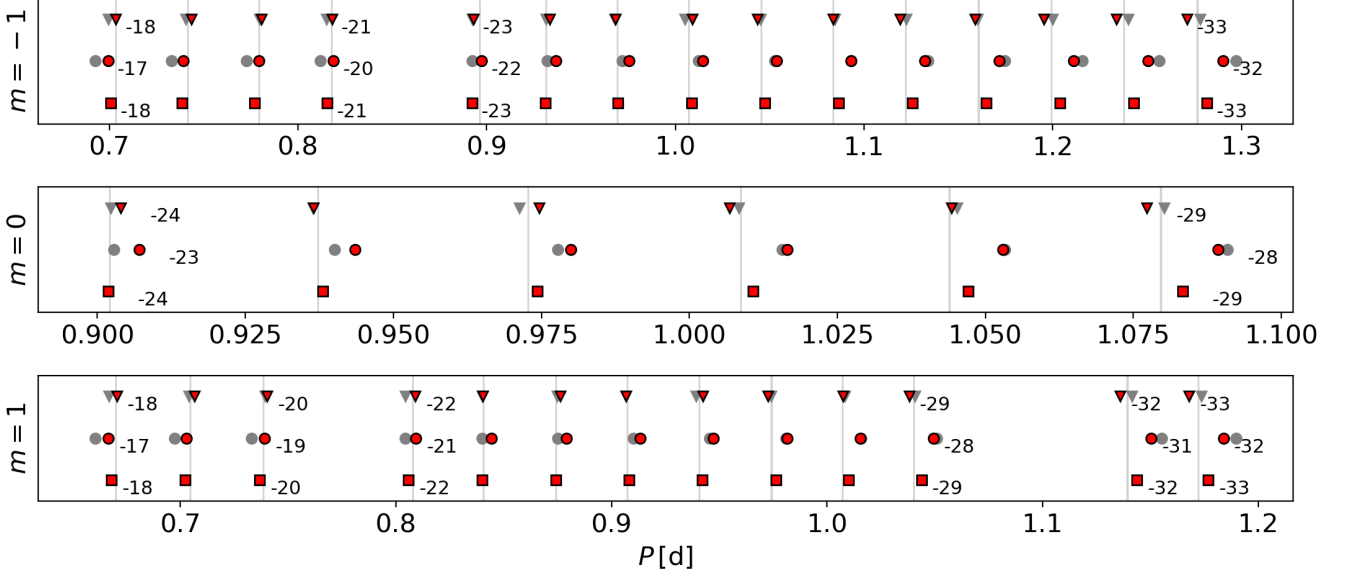
Figure 8. Observed mode periods of KIC 9751996 indicated as gray vertical lines from Van Reeth et al. (2015), the uncertainties on the measured mode periods are too small to be seen at this scale. The symbols represent the theoretical predicted mode periods of the best-fitting models in each grid. Triangles: Model without diffusion and $Z_{\rm ini}$ according to the spectroscopically derived value (model M02). Circles: Model with diffusion and $Z_{\rm ini}$ according to the spectroscopically derived value (model M04). Squares: Model with diffusion and $Z_{\rm ini}$ fixed at 0.014 (model M05). Radial orders of the modes are indicated next to the symbols. The gray symbols indicate the mode periods of models M01 and M03.
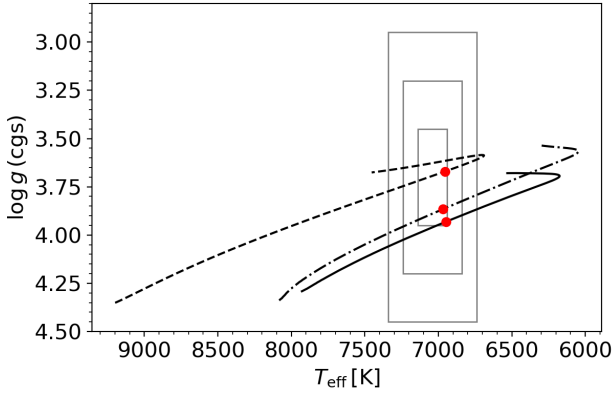
Figure 9. Evolution tracks for the best model with atomic diffusion (black solid line, model M04) and best model without diffusion (black dashed line, model M02) for KIC 9751996. The evolution track of the best model for with atomic diffusion and $Z_{\rm ini} = 0.014$ is indicated with the black dashed-dotted line (model M05). The red dots indicate the predicted $T_{\rm eff}$ and $\log g$ for each of the models. The gray boxes mark the 1-, 2-, and 3-σ spectroscopic uncertainties.

The corresponding periods and evolution tracks of the best models (M04 and M05) with atomic diffusion (spectroscopic and solar metallicity) are shown in Fig. 8 and Fig. 9, respectively. Fig. 8 also shows the predicted mode periods from model M03 (gray circles). Based on the difference in the value of the AIC, ΔAIC, the
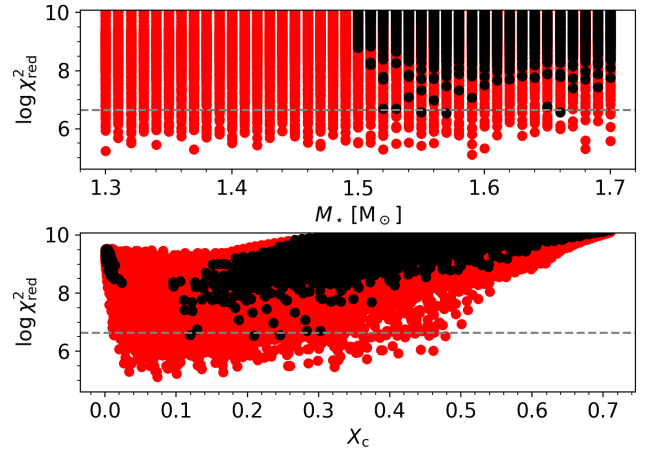

Figure 10. Reduced χ^2 distributions when modeling KIC 11145123 with the grid without diffusion where $Y_{\rm ini} = 1 - X_{\rm ini} - Z_{\rm ini}$. The red dots indicate the models which have been eliminated since these do not agree with the 1-σ uncertainty on $T_{\rm eff}$ and 3-σ uncertainty on $\log g$. The dashed gray line indicates the 1-σ confidence interval for the black dots.

models without atomic diffusion is strongly favored over the models without diffusion. In particular, for both choices of initial composition a model without atomic diffusion gives a better result. In Fig. 15, we show the cumulative $\chi^2_{\rm red}$ distributions of the three grids for the
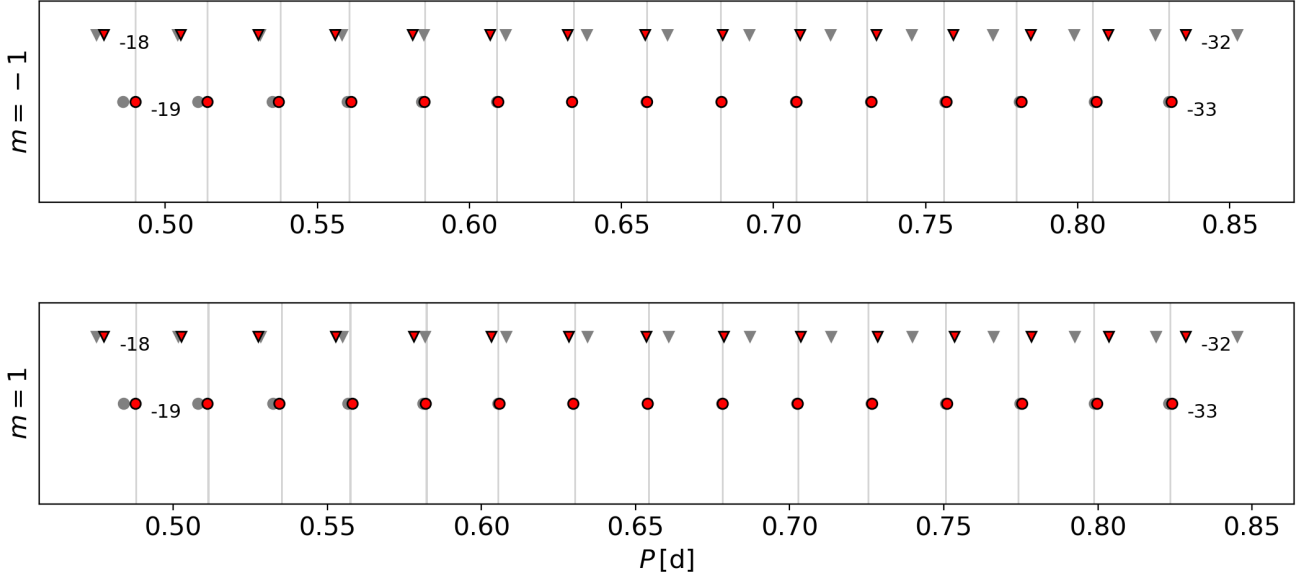
Figure 11. Observed mode periods of KIC 11145123 indicated as gray vertical lines from Kurtz et al. (2014), the uncertainties on the measured mode periods are too small to be seen at this scale. The symbols represent the theoretical predicted mode periods of the best-fitting models in each grid. Triangles: Model without diffusion and $Z_{\rm ini}$ according to the spectroscopically derived value according to Takada-Hidai et al. (2017) (model M06). Circles: Model with diffusion and $Z_{\rm ini}$ according to the spectroscopically derived value (model M08). Radial orders of the modes are indicated next to the symbols. The gray symbols indicate the mode periods of models M07 and M09.

	KIC 9751996					KIC 11145123				
Model ID	M01	M02	M03	M04	M05	M06	M07	M08	M09	M10
Diffusion	No	No	Yes	Yes	Yes	No	No	Yes	Yes	Yes
$M_\star\,[{\rm M_\odot}]$	1.71	1.90	1.89	1.80	1.68	1.57	1.66	1.36	1.43	-
$X_{\rm c}$	0.256	0.103	0.292	0.314	0.286	0.209	0.292	0.058	0.095	-
$X_{\rm ini}$	0.715	0.698	0.715	0.707	0.715	0.715	0.752	0.715	0.749	0.715
$Y_{\rm ini}$	0.259	0.276	0.263	0.271	0.271	0.283	0.246	0.283	0.248	0.271
$Z_{\rm ini}$	0.026	0.026	0.022	0.022	0.014	0.002	0.002	0.002	0.003	0.014
$f_{\rm ov}$	0.0100	0.0175	0.0100	0.0175	0.0300	0.0100	0.0100	0.0225	0.0100	-
$\log \chi^2_{\rm red}$	4.23	4.22	5.45	5.18	4.45	6.54	7.79	5.34	5.50	-
$\tau\,[{\rm Gyr}]$	1.290	1.139	1.116	1.297	1.689	1.484	1.402	2.234	2.075	-
$M_{\rm cc}\,[{\rm M_\odot}]$	0.177	0.169	0.190	0.189	0.193	0.100	0.103	0.132	0.121	-
$T_{\rm eff}\,[{\rm K}]$	7137	6953	7110	6948	6968	7461	7562	7622	7574	-
$\log g\,({\rm cgs})$	3.95	3.67	3.94	3.93	3.87	4.10	4.13	3.88	4.02	-
$\Pi_0\,[{\rm s}]$	4438	4438	4639	4653	4475	3086	3248	2999	2972	-
$\Pi_0^{\rm (obs)}\,[{\rm s}]$			4364 ± 7					2945 ± 78		

Table 2. Best-fitting parameters for both KIC 9751996 and KIC 11145123 when only models within 1σ (3σ for $\log g$ in case of KIC 11145123) of the spectroscopically derived values of $T_{\rm eff}$ and $\log g$ are considered. All parameters listed below the reduced χ^2 follow from the model and are thus not free parameters. When the metallicity is set according to the spectroscopic value, we list both solutions for the two different relations to set $X_{\rm ini}$ and $Y_{\rm ini}$, as discussed in Sec. 2. For KIC 11145123, the grid with fixed $Z_{\rm ini} = 0.014$ does not yield solutions consistent with the spectroscopic $T_{\rm eff}$ and $\log g$. The bottom rows lists the measured values of Π_0 from Van Reeth et al. (2016) and Kurtz et al. (2014) for KIC 9751996 and KIC 11145123, respectively.
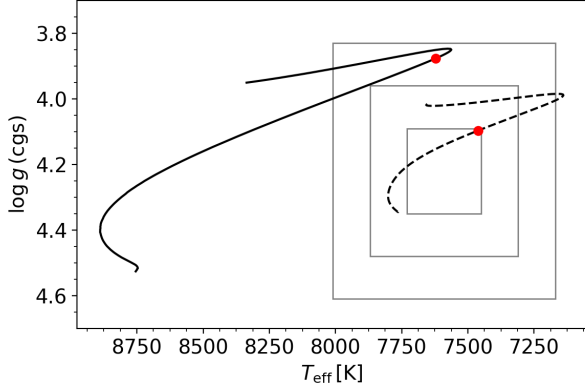
Figure 12. Same as Fig. 9, but for KIC 11145123. The spectroscopic $T_{\rm eff}$ and $\log g$ are taken from Takada-Hidai et al. (2017), where the more conservative uncertainty on $T_{\rm eff}$ (Table 3) is taken.
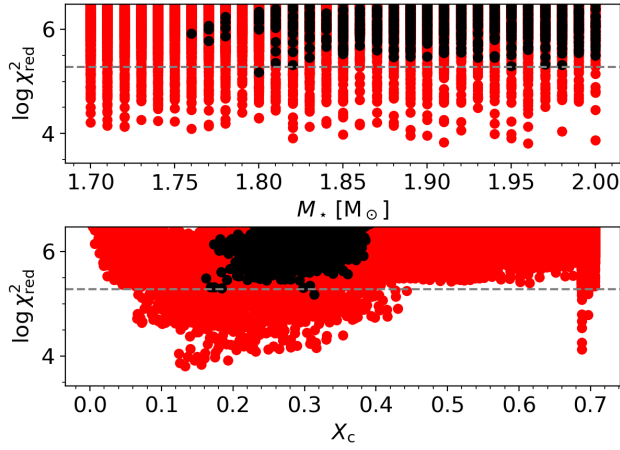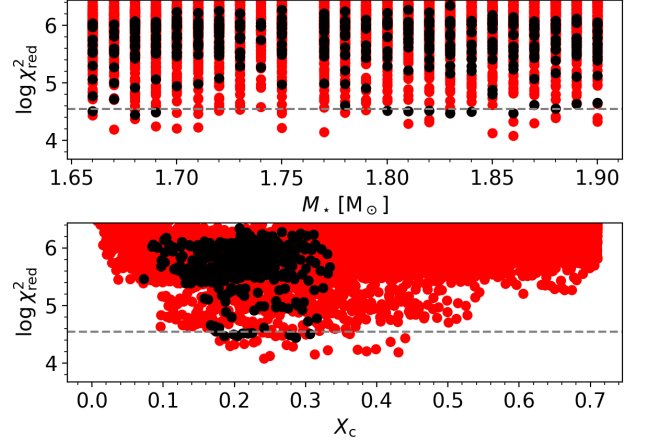

Figure 14. Same as Fig. 21 (KIC 9751996), but for the grid with atomic diffusion included and a metallicity fixed at $Z_{\rm ini} = 0.014$.

Figure 13. Same as Fig. 7 (KIC 9751996), but for the grid with atomic diffusion included and a metallicity according to the spectroscopically derived value.

best 20 models. It can be seen that the grid with atomic diffusion with the metallicity set according to the spectroscopic value does not give a more accurate fit. About a quarter of the best models without atomic diffusion give a better match than the best models with atomic diffusion and $Z_{\rm ini} = 0.014$.

Additionally, we study the star's surface abundances and compare these with the predictions from our best models. There are no abundance measurements available for KIC 9751996 available in the literature. Moreover, the spectra of KIC 9751996 used in the study by Van Reeth et al. (2016) do not have the required signal-to-noise ratio (SNR) to derive surface abundances. Therefore, four additional spectra – each with an exposure time of 2700 sec – were taken on 2019 May 24-25
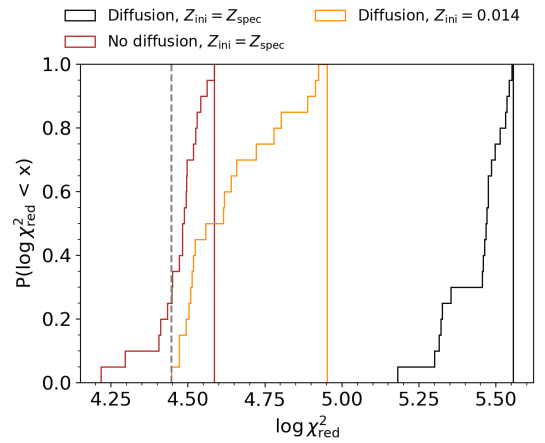

Figure 15. The $\log \chi^2_{\rm red}$ cumulative distributions of the best 20 models from each grid (corresponding to models M02, M04, and M05) for KIC 9751996. As a visual aid, a dashed line is plotted at the $\log \chi^2_{\rm red}$ value of the best model from the grid where atomic diffusion is included, and the metallicity fixed at $Z_{\rm ini} = 0.014$.

with the High Efficiency and high Resolution Mercator Échelle Spectrograph (HERMES, Raskin et al. 2011) on the 1.2-m Mercator telescope (La Palma, Spain). The spectra were taken with the HERMES high-resolution fiber, yielding a resolution of $R = 85\,000$. After normalization, the average spectrum is calculated. This normalized spectrum was fitted with synthetic spectra deduced from atmosphere models. First, a global solution was found for the effective temperature $T_{\rm eff}$, surface gravity $\log g$, projected surface velocity $v \sin i$, metallicity [M/H], and microturbulence ξ, using the GSSP software package (Tkachenko 2015), where we use
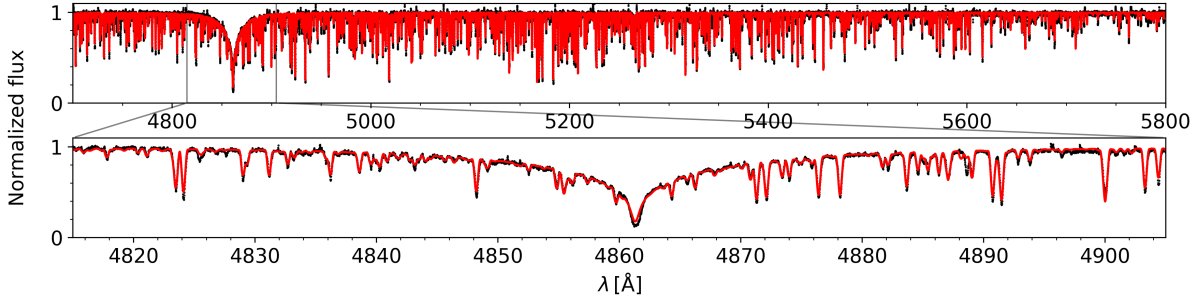
Figure 16. The best-fitting synthetic spectrum (red) for the normalized averaged spectrum of KIC 9751996 (black). The bottom panel shows a zoom-in around the Hβ line.

the spectrum between 4700 and 5800 Å. The parameters of the global solution and the measured surface abundances are presented in Table 3 and a plot of the best fitting synthetic spectrum is shown in Fig. 16. Our atmospheric parameters for the global solution are consistent within 1σ compared to those by Van Reeth et al. (2015). Subsequently, the parameters of the global solution are fixed, and individual surface abundances are determined. The results are presented in Table 4 which have been used as a check after the best asteroseismic models were selected.

Fig. 17 shows the predicted surface abundances and the observed abundances of elements for which radiative levitations have been computed. We refer to Appendix B for the conversion of the abundances from $\log(n_X/n_{tot})$ to [X/H]. Regarding the theoretically predicted abundances, we point out that the sharp variations seen in some of the elements have a numerical origin, as at these points $g_{rad,i}$ is of the same order as g. This behavior is one of the reasons why we refrain from including the surface abundances in the selection scheme, as only the global trend should be trusted. Since the constant chemical mixing in the stellar envelope is at a low level to keep compliance with the g-mode trapping properties (Van Reeth et al. 2016), the surface abundances of the models without atomic diffusion will remain constant throughout the MS evolution. The best model without atomic diffusion (solar mixture as per Asplund et al. (2009)) is not able to explain all observed surface abundances within the 2-σ intervals. Yet, the models with atomic diffusion do not give more accurate predictions. Hence, the surface abundances do not help to improve the asteroseismic best model fit for in the case of KIC 9751996.

4.2.2. KIC 11145123

When T_{eff} and $\log g$ are taken as additional input parameters, along with the g-mode periods, we find that the model with the spectroscopic metallicity is consistent with the 1- and 3-σ uncertainty intervals of T_{eff} and $\log g$, respectively. However, the best model obtained for

Parameter	Value KIC 11145123	Value KIC 9751996	Closest grid point
T_{eff} [K]	7590^{+80}_{-140}	7040 ± 100	7100
$\log g$ (cgs)	4.22 ± 0.13	3.70 ± 0.25	3.70
$v \sin i$ [km s^{-1}]	$5.9 \pm 0.2^{\dagger}$	12.5 ± 0.7	12
[M/H]	-0.71 ± 0.11	0.20 ± 0.07	0.2
ξ [km s^{-1}]	3.1 ± 0.5	3.16 ± 0.30	3.3

Table 3. Parameters for the best spectroscopic model of KIC 11145123 according to Takada-Hidai et al. (2017) and KIC 9751996 from this work using GSSP. The fourth column lists the value of the grid point closest to the best solution listed in the previous column. The listed [M/H] values are scaled by assuming $Z_\odot = 0.0134$ as per Asplund et al. (2009). †Apparent projected rotation velocity.

Element	$\log(n_X/n_{tot})$
C	$-3.64^{+0.19}_{-0.23}$
O	<-2.8
Na	$-5.52^{+0.25}_{-0.27}$
Mg	$-4.43^{+0.11}_{-0.12}$
Si	$-4.48^{+0.19}_{-0.27}$
S	<-4.41
Ca	$-5.95^{+0.20}_{-0.21}$
Sc	$-9.22^{+0.29}_{-0.35}$
Ti	$-7.06^{+0.11}_{-0.11}$
Cr	$-6.06^{+0.08}_{-0.09}$
Mn	$-6.44^{+0.21}_{-0.23}$
Fe	$-4.42^{+0.04}_{-0.04}$
Y	$-9.68^{+0.22}_{-0.25}$
Ni	$-5.47^{+0.08}_{-0.08}$

Table 4. Measured surface abundances, in number density per total number density, of KIC 9751996 by fixing the parameters of the global solution listed in Table 3.

$Z_{ini} = 0.014$ is inconsistent with these intervals. Table 2 lists the best models when we demand compliance with the spectroscopy. The grid with Z_{ini} according to the spectroscopic surface metallicity returns a model that is
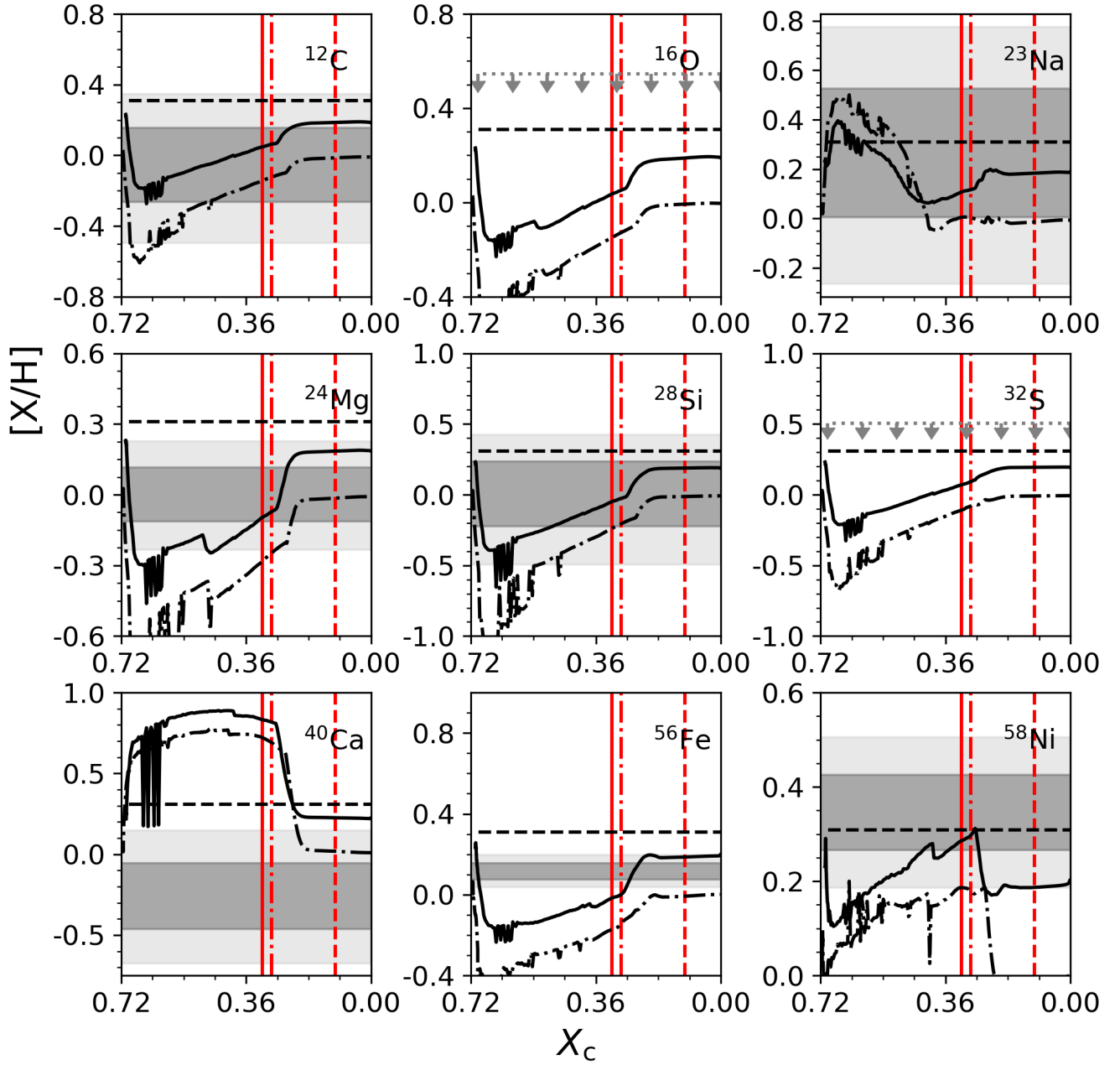
Figure 17. The evolution of the surface abundances of the best models M02, M04, and M05 for KIC 9751996. *Solid line:* Model with atomic diffusion and $Z_{\rm ini}$ according to the spectroscopic value from Van Reeth et al. (2016). *Dashed line:* Model without diffusion and $Z_{\rm ini}$ according to the spectroscopic value. *Dashed-dotted line:* Model with diffusion and $Z_{\rm ini} = 0.014$. The $1(2)$-σ intervals are shown as dark (light) shaded regions. For O and S, only the upper limits could be inferred. The red lines indicate the estimate of $X_{\rm c}$ for each model, where the same line style convention is used.

near the TAMS, as predicted by Kurtz et al. (2014) (cf.
Fig. 18). The corresponding model pulsation periods
are shown in Fig 11, and the evolution track is shown
in Fig. 12. If $Z_{\rm ini} = 0.014$ is assumed, no models can be
found within the aforementioned spectroscopic intervals.
We find that the grid with atomic diffusion gives a better
fit compared to grid without, and is significantly more
probable of reproducing the data according to the AIC.
From Fig. 19, it can be seen that all of the 20 best mod-
els with atomic diffusion give smaller χ^2 values than the
best model without atomic diffusion. The conclusion on
whether atomic diffusion improves the modeling of the
oscillations is independent of the two choices of the ini-
tial composition. The predicted surface abundances of
the model with atomic diffusion is able to explain the
Na and Ni surface abundances, whereas the model with-
out atomic diffusion cannot, as shown in Fig. 20. The
observed abundances of O, Si, S, and Ca are not repro-
duced by either model, which might be the result of the
star having a different chemical mixture than the Sun.
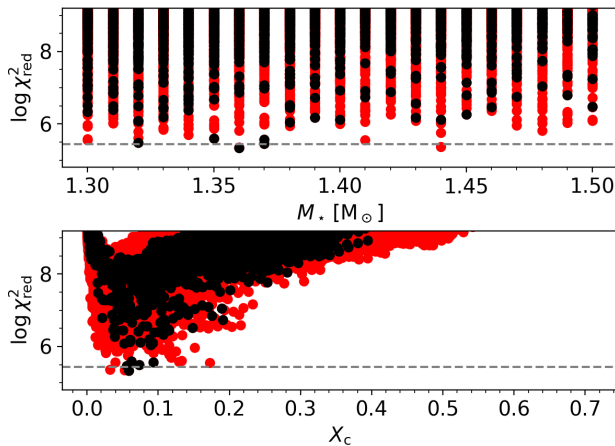
Figure 18. Same as Fig. 10 (KIC 11145123), but for the grid
with atomic diffusion included and a metallicity according to
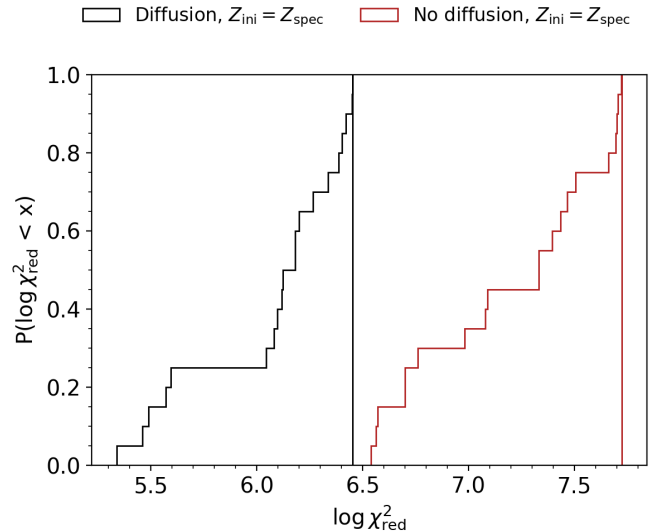the spectroscopically derived value.

Figure 19. The $\log \chi^2_{\rm red}$ probability distributions of the best
20 models from each grid (corresponding to models M06 and
M08) for KIC 11145123 (no consistent models found for the
grid with solar metallicity).

5. CONCLUSION & DISCUSSION

This work sheds light on four important questions re-
garding the asteroseismic modeling of slowly rotating γ
Doradus (A/F-type) pulsators. We investigated the ef-
fect of including the process of atomic diffusion, with
accelerations induced by radiative levitation included,
in the equilibrium models for intermediate-mass stars,
and the consequence for the frequencies of the g modes.
The shifts in pulsation frequencies when these are com-
puted from an equilibrium model where atomic diffu-
sion is included are typically detectable with photomet-
ric data with time base of 1-year or longer. Although we
have limited ourselves to stars which have a low rotation
rate, atomic diffusion will most likely also be a dom-
inant chemical element transport mechanism in faster
rotating stars. A recent study by Deal et al. (2020) has
found that atomic diffusion dominates over rotationally
induced mixing in stars $M_\star > 1.4 \, {\rm M_\odot}$ for rotation ve-
locities between 30 and 80 km s^{-1}.

We have investigated the gain in constraining power
when using the periods of the individual observed pulsa-
tions instead of the reduced asymptotic period spacing,
Π_0, as asteroseismic input (Mombarg et al. 2019). When
using the individual periods, the effective temperature
$T_{\rm eff}$ and surface gravity $\log g$ are used to eliminate mod-
els a posteriori that are inconsistent within the measured
intervals of these observables. This study is the first to
perform asteroseismic modeling of individual g modes in
single γ Dor pulsators, where we have used two slowly-
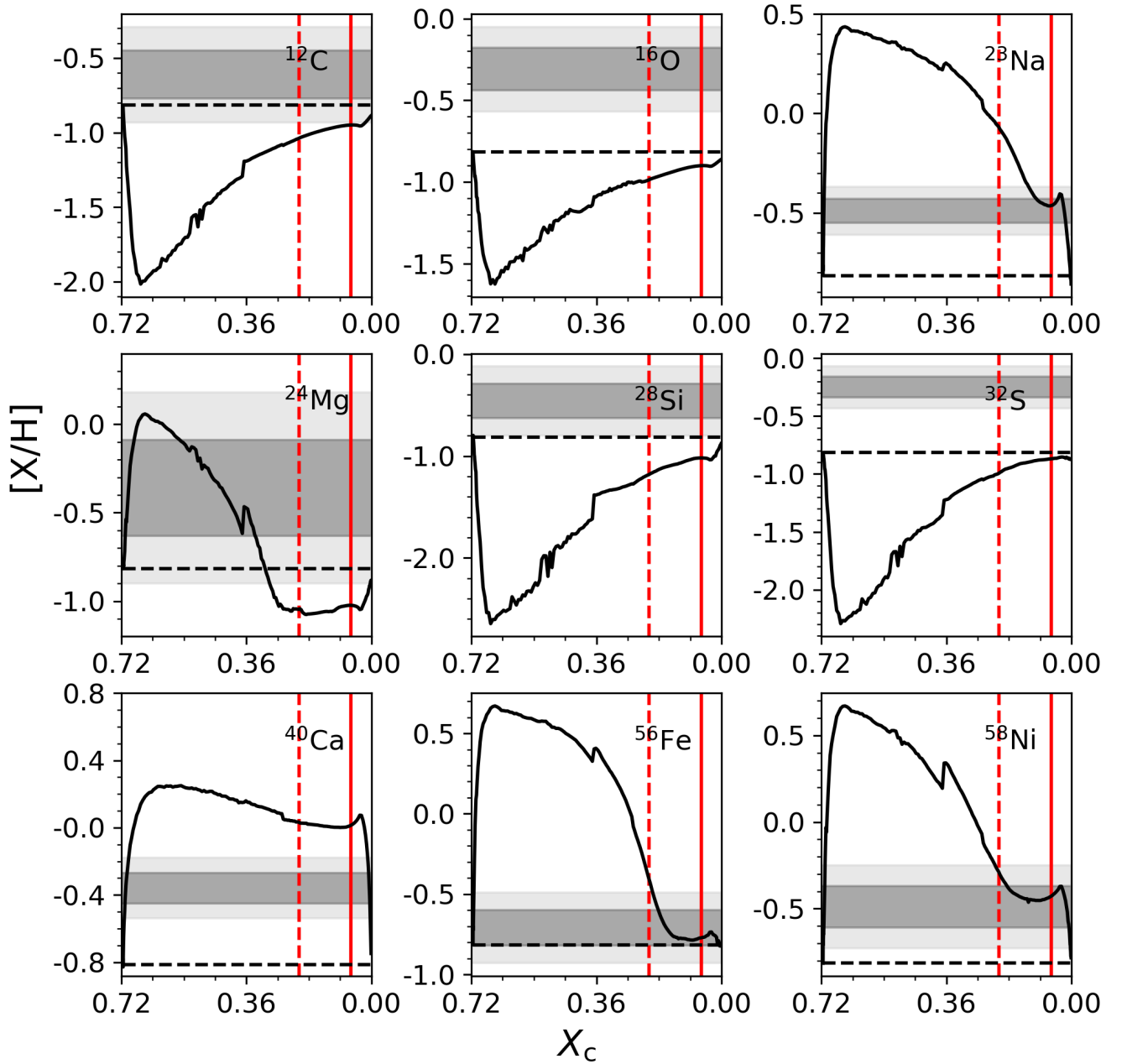rotating test stars observed by the nominal *Kepler* mis-

Figure 20. The evolution of the surface abundances of the best models M06 and M08 (no solution for $Z_{\mathrm{ini}} = 0.014$) for KIC 11145123. *Solid line:* Model with atomic diffusion and Z_{ini} according to the spectroscopic value from Takada-Hidai et al. (2017). *Dashed line:* Model without diffusion and Z_{ini} according to the spectroscopic value. The 1(2)-σ intervals from Takada-Hidai et al. (2017) are shown as dark (light) shaded regions. The red lines indicate the estimate of X_{c} for each model, where the same line style convention is used.

sion: KIC 9751996 (Van Reeth et al. 2015, 2016) and KIC 11145123 (Kurtz et al. 2014; Takada-Hidai et al. 2017). The use of the individual pulsations does allow us to improve upon the X_c estimates compared to the method from Mombarg et al. (2019), but degeneracies between the mass and metallicity do not allow us to refine the mass of the star. The best model without atomic diffusion yields a mass $M_\star = 1.90\,\mathrm{M}_\odot$ and $X_c = 0.103$ for KIC 9751996, which are both consistent with $M_\star = 1.95 \pm 0.10\,\mathrm{M}_\odot$ and $X_c = 0.14^{+0.07}_{-0.09}$ from Π_0 instead of the individual mode periods.

We have modeled KIC 9751996 and KIC 11145123 from grids of stellar evolution models where the process of atomic diffusion (including radiative levitations) has been taken into account. The difference in inferred masses between models with and without atomic diffusion are typically larger than the $0.1\,\mathrm{M}_\odot$ uncertainty Mombarg et al. (2019) found from ensemble modeling of 37 γ Dor stars using (Π_0, T_eff, $\log g$). Furthermore, we have investigated if the observed surface metallicities of these two stars have been altered by atomic diffusion, assuming the stars had an initial metallicity close to the solar value (i.e. fixed at $Z_\mathrm{ini} = 0.014$). Based on the Akaike Information Criterion (AIC), and the χ^2_red distributions of the best 20 models, we found that models without atomic diffusion are favored in the case of KIC 9751996. For this star, we find a well-matching fit without including atomic diffusion, given the typical uncertainties on theoretically predicted periods for A/F stars. Atomic diffusion should occur in stars, hence our finding that models without it perform better but cannot fit the observed mode periods up to the measurement errors implies that other transport processes must be at work in this star. For KIC 11145123, we found that this initial solar metallicity scenario does not yield any models consistent within the spectroscopic uncertainties derived by Takada-Hidai et al. (2017). Yet, when the initial metallicity is set according to the spectroscopic value found by these authors, we found $M_\star = 1.36$ and $X_c = 0.058$, which is in line with the prediction based on the average period spacing by Kurtz et al. (2014). For this star, including atomic diffusion improves the fit to an acceptable level, without any need to consider a binary merger models – as proposed by Takada-Hidai et al. (2017) – from the viewpoint of g-mode asteroseismology.

The depth of our g-mode modeling is superior to any previous modeling of A/F-type pulsators in the literature. Moreover, we have investigated two options to choose Y_ini (when Z_ini is fixed at the spectroscopic value): fixing X_ini or use an enrichment rate (Verma et al. 2019). For both stars our conclusion whether in-

cluding atomic diffusion improves upon the fit to the observed g-mode periods does not depend on which of these two options is chosen.

In this work we have investigated whether the measured surface abundances of C, O, Na, Mg, Si, S, Ca, Fe, and Ni (for KIC 11145123 taken from Takada-Hidai et al. (2017)) are able to distinguish between models with and without atomic diffusion. As the predictive power of surface abundances is quite weak compared to gravity modes, we have only used these as an extra check, rather than fitting these. For KIC 9751996, this comparison was inconclusive, while for KIC 11145123 the model with atomic diffusion was able to explain more of the measured abundances, although not all of them could be matched.

The star KIC 11145123 is a special case, as not all of the asteroseismic and spectroscopic findings by Kurtz et al. (2014) and Takada-Hidai et al. (2017), respectively, can be explained. The latter study argued that KIC 11145123 is most likely not a member of the thin disk, as these authors estimate the star to be located roughly 400 pc above the galactic plane, i.e. close to the edge of the thin disk. However, these estimates were based on a distance estimate from the seismic luminosity (Kurtz et al. 2014). Now that the parallax and proper motion are available from the Gaia DR2 release (Gaia Collaboration et al. 2016, 2018), we find that KIC 11145123 is about 260 pc away from the galactic plane. Furthermore, we find a peculiar velocity of about 72 km s^{-1} by using the formalism from Moffat et al. (1998), indicating KIC 11145123 might be a runaway star. Our best model with atomic diffusion is not able to explain the high observed [O/Fe] surface abundance, nor can the model with diffusion starting out at solar metallicity account for the low observed surface metallicity.

Stellar evolution models with atomic diffusion will be important for asteroseismic modeling of a large sample of γ Dor stars. The tests done in this work will be repeated for the sample in Van Reeth et al. (2016, 2018) in a forthcoming paper.

Facilities: Mercator (HERMES)

Software: MESA (r11701; Paxton et al. 2011, 2013, 2015, 2018, 2019), GSSP (Tkachenko 2015), GYRE (v5.2; Townsend & Teitler 2013; Townsend et al. 2018)

APPENDIX

A. ALTERNATIVE FITTING METHODS AND INITIAL CONDITIONS

In this section we present the best models when $T_{\rm eff}$ and $\log g$ are included into the fit, which in most cases still yields models that are inconsistent within the 1-σ intervals of these input parameters. For KIC 11145123, we also listed the best models when 1-σ intervals for both $T_{\rm eff}$ and $\log g$ are used to eliminate models after fitting the pulsations.

KIC 9751996			
Spectroscopy	Fit	Fit	Fit
Diffusion	No	Yes	Yes
$M_\star\,[{\rm M_\odot}]$	1.67	1.65	1.86
$X_{\rm c}$	0.293	0.410	0.242
$X_{\rm ini}$	0.715	0.715	0.715
$Y_{\rm ini}$	0.259	0.255	0.271
$Z_{\rm ini}$	0.026	0.030	0.014
$f_{\rm ov}$	0.0100	0.0175	0.0100
$\log \chi^2_{\rm red}$	4.08	3.71	4.05
$\tau\,[{\rm Gyr}]$	1.300	1.641	1.060
$M_{\rm cc}\,[{\rm M_\odot}]$	0.177	0.152	0.194
$\Pi_0\,[{\rm s}]$	4444	4565	4440
$T_{\rm eff}\,[{\rm K}]$	7157	6489	7563
$\log g\,({\rm cgs})$	3.99	4.07	3.93

Table 5. Best-fitting parameters for KIC 9751996 when the $T_{\rm eff}$ and $\log g$ derived from high-resolution spectroscopy are included into the χ^2. All parameters listed below the reduced χ^2 follow from the model and are thus not free parameters.

KIC 11145123						
Spectroscopy	Fit	Fit	Fit	Cutoff	Cutoff	Cutoff
Diffusion	No	Yes	Yes	No	Yes	Yes
$M_\star\,[{\rm M_\odot}]$	1.59	1.36	1.47	1.57	1.30	-
$X_{\rm c}$	0.073	0.058	0.028	0.209	0.148	-
$X_{\rm ini}$	0.715	0.715	0.715	0.715	0.715	0.715
$Y_{\rm ini}$	0.283	0.283	0.271	0.283	0.282	0.271
$Z_{\rm ini}$	0.002	0.002	0.014	0.002	0.003	0.014
$f_{\rm ov}$	0.0225	0.0225	0.0225	0.0100	0.0100	-
$\log \chi^2_{\rm red}$	5.09	5.34	5.47	6.54	6.52	-
$\tau\,[{\rm Gyr}]$	2.003	2.234	2.973	1.484	2.151	-
$M_{\rm cc}\,[{\rm M_\odot}]$	0.114	0.132	0.099	0.100	0.116	-
$\Pi_0\,[{\rm s}]$	3024	2999	3090	3086	2982	-
$T_{\rm eff}\,[{\rm K}]$	6734	7622	6056	7461	7604	-
$\log g\,({\rm cgs})$	3.83	3.88	3.79	4.10[†]	4.11[†]	-

Table 6. Best-fitting parameters for KIC 11145123 when the $T_{\rm eff}$ and $\log g$ for spectroscopy are included into the χ^2. All parameters listed below the reduced χ^2 follow from the model and are thus not free parameters. [†]Enforced to comply with the 1-σ uncertainty interval.
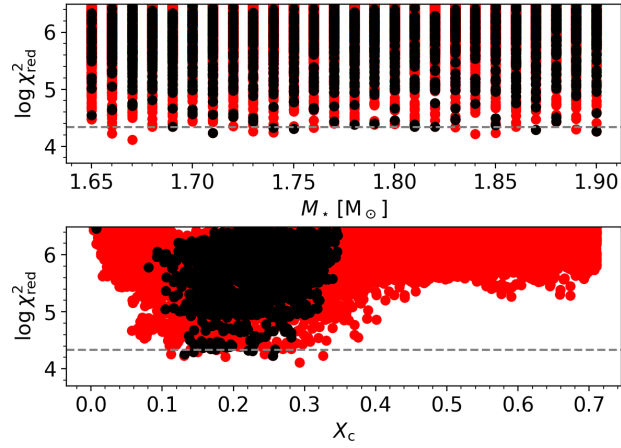
Figure 21. Reduced χ^2 distributions when modeling KIC 9751996 with the grid without diffusion where $Y_{ini} = 1 - X_{ini} - Z_{ini}$. The red dots indicate the models which have been eliminated since these do not agree with the 1-σ uncertainties on T_{eff} and $\log g$. The dashed gray line indicates the 1-σ confidence interval for the black dots.

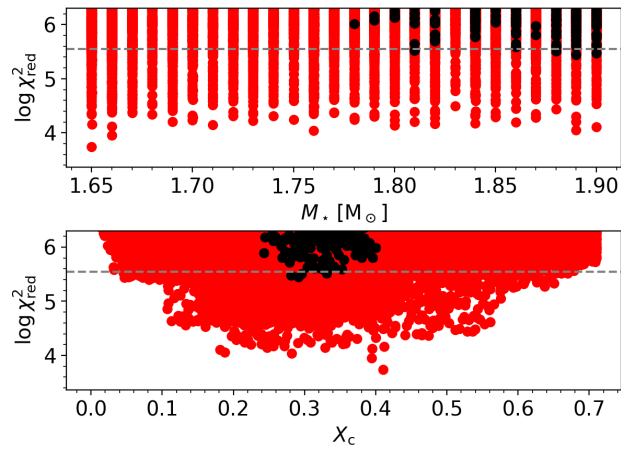**Figure 22.** Same as Fig. 21 (KIC 9751996), but for the grid with atomic diffusion included and a metallicity according to the spectroscopically derived value.
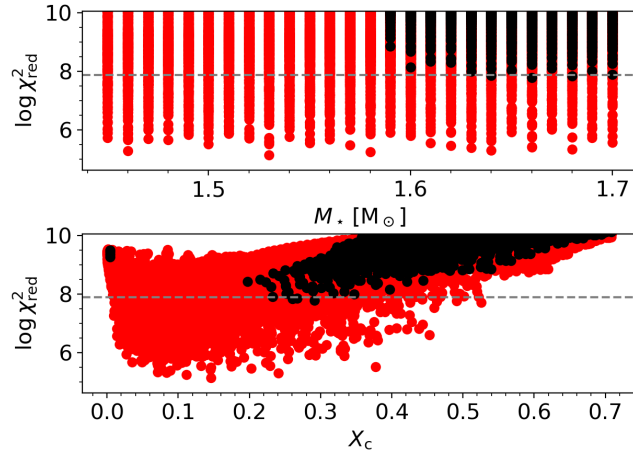
Figure 23. Reduced χ^2 distributions when modeling KIC 11145123 with the grid without diffusion where $Y_{\rm ini}$ is set as per Verma et al. (2019). The red dots indicate the models which have been eliminated since these do not agree with the 1-σ uncertainty on $T_{\rm eff}$ and 3-σ uncertainty on $\log g$. The dashed gray line indicates the 1-σ confidence interval for the black dots.
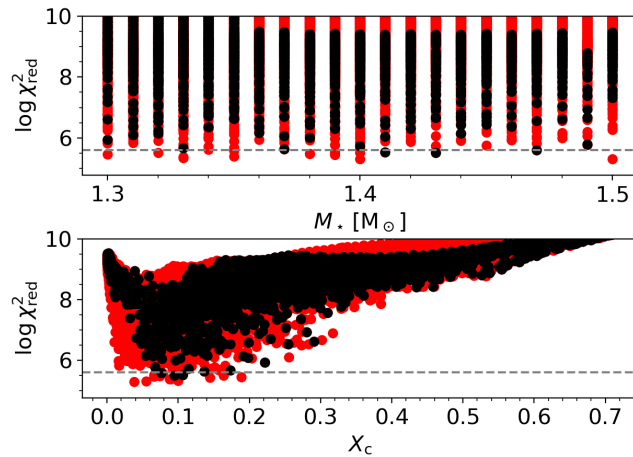

Figure 24. Same is Fig. 23 (KIC 11145123), but for the grid with atomic diffusion included and a metallicity according to the spectroscopically derived value.

B. CONVERSION OF ABUNDANCES

Below, we show how the abundances from GSSP, given in $\log(n_X/n_{tot})$, have been converted to [X/H] in order to make a comparison with the abundances predicted by the theoretical models. Firstly, the abundances are converted to n_X/n_H using

$$\log\left(\frac{n_X}{n_{tot}}\right) - \log\left(\frac{n_X}{n_{tot}}\right)_\odot = \log\left(\frac{n_X}{n_H}\right) + \log\left(\frac{n_H}{n_{tot}}\right) - \log\left(\frac{n_X}{n_H}\right)_\odot - \log\left(\frac{n_H}{n_{tot}}\right)_\odot , \tag{B1}$$

where n_H is the number density of hydrogen. Next, we assume $\log(n_H/n_{tot}) \approx \log(n_H/n_{tot})_\odot$, such that

$$\log\left(\frac{n_X}{n_H}\right) = \log\left(\frac{n_X}{n_{tot}}\right) - \log\left(\frac{n_H}{n_{tot}}\right)_\odot . \tag{B2}$$

Finally,

$$[X/H] = \log\left(\frac{n_X}{n_H}\right) - \log\left(\frac{n_X}{n_H}\right)_\odot \tag{B3}$$

$$= \log\left(\frac{n_X}{n_{tot}}\right) - \log\left(\frac{n_H}{n_{tot}}\right)_\odot - \log\epsilon_{X,\odot} + 12. \tag{B4}$$

REFERENCES

Aerts, C., Christensen-Dalsgaard, J., & Kurtz, D. W. 2010, Asteroseismology, A & A Library, Springer-Verlag, Heidelberg

Aerts, C., Mathis, S., & Rogers, T. M. 2019a, ARA&A, 57, 35

Aerts, C., Molenberghs, G., Michielsen, M., et al. 2018, ApJS, 237, 15

Aerts, C., Pedersen, M. G., Vermeyen, E., et al. 2019b, A&A, 624, A75

Alecian, G., & LeBlanc, F. 2002, MNRAS, 332, 891

Asplund, M., Grevesse, N., Sauval, A. J., & Scott, P. 2009, ARA&A, 47, 481

Auvergne, M., Bodin, P., Boisnard, L., et al. 2009, A&A, 506, 411

Borucki, W. J., Koch, D., Basri, G., et al. 2010, Science, 327, 977

Bowman, D. M., Burssens, S., Pedersen, M. G., et al. 2019, Nature Astronomy, 3, 760

Burgers, J. M. 1969, Flow Equations for Composite Gases

Choi, J., Dotter, A., Conroy, C., & Ting, Y.-S. 2018, ApJ, 860, 131

Christensen-Dalsgaard, J., Proffitt, C. R., & Thompson, M. J. 1993, ApJL, 403, L75

Deal, M., Alecian, G., Lebreton, Y., et al. 2018, A&A, 618, A10

Deal, M., Goupil, M. J., Marques, J. P., Reese, D. R., & Lebreton, Y. 2020, A&A, 633, A23

Deal, M., Richard, O., & Vauclair, S. 2016, A&A, 589, A140

Dotter, A., Conroy, C., Cargile, P., & Asplund, M. 2017, ApJ, 840, 99

Eckart, C. 1960, Physics of Fluids, 3, 421

Freytag, B., Ludwig, H. G., & Steffen, M. 1996, A&A, 313, 497

Gaia Collaboration, Prusti, T., de Bruijne, J. H. J., et al. 2016, A&A, 595, A1

Gaia Collaboration, Brown, A. G. A., Vallenari, A., et al. 2018, A&A, 616, A1

Glaspey, J. W., Pritchet, C. J., & Stetson, P. B. 1994, AJ, 108, 271

Guzik, J., Fontes, C., & Fryer, C. 2018, Atoms, 6, 31

Hu, H., Tout, C. A., Glebbeek, E., & Dupret, M.-A. 2011, MNRAS, 418, 195

Hui-Bon-Hoa, A., & Vauclair, S. 2018, A&A, 610, L15

Johnston, C., Aerts, C., Pedersen, M. G., & Bastian, N. 2019a, A&A, 632, A74

Johnston, C., Tkachenko, A., Aerts, C., et al. 2019b, MNRAS, 482, 1231

Kahraman Aliçavuş, F., Niemczura, E., De Cat, P., et al. 2016, MNRAS, 458, 2307

Kass, R. E., & Raftery, A. E. 1995, Journal of the American Statistical Association, 90, 773

Kurtz, D. W., Saio, H., Takata, M., et al. 2014, MNRAS, 444, 102

LeBlanc, F., & Alecian, G. 2004, MNRAS, 352, 1329

LeBlanc, F., Michaud, G., & Richer, J. 2000, ApJ, 538, 876

Li, G., Bedding, T. R., Murphy, S. J., et al. 2019a, MNRAS, 482, 1757

Li, G., Van Reeth, T., Bedding, T. R., et al. 2019b, MNRAS, 2517

Maeder, A. 2009, Physics, Formation and Evolution of Rotating Stars, doi:10.1007/978-3-540-76949-1

Michaud, G., Alecian, G., & Richer, J. 2015, Atomic Diffusion in Stars, A & A Library, Springer International Publishing Switzerland

Michielsen, M., Pedersen, M. G., Augustson, K. C., Mathis, S., & Aerts, C. 2019, A&A, 628, A76

Moffat, A. F. J., Marchenko, S. V., Seggewiss, W., et al. 1998, A&A, 331, 949

Mombarg, J. S. G., Van Reeth, T., Pedersen, M. G., et al. 2019, MNRAS, 485, 3248

Moravveji, E., Aerts, C., Pápics, P. I., Triana, S. A., & Vandoren, B. 2015, A&A, 580, A27

Moravveji, E., Townsend, R. H. D., Aerts, C., & Mathis, S. 2016, ApJ, 823, 130

Morel, P., & Thévenin, F. 2002, A&A, 390, 611

Ouazzani, R. M., Marques, J. P., Goupil, M. J., et al. 2019, A&A, 626, A121

Pápics, P. I., Moravveji, E., Aerts, C., et al. 2014, A&A, 570, C4

Paquette, C., Pelletier, C., Fontaine, G., & Michaud, G. 1986, ApJS, 61, 177

Paxton, B., Bildsten, L., Dotter, A., et al. 2011, ApJS, 192, 3

Paxton, B., Cantiello, M., Arras, P., et al. 2013, ApJS, 208, 4

Paxton, B., Marchant, P., Schwab, J., et al. 2015, ApJS, 220, 15

Paxton, B., Schwab, J., Bauer, E. B., et al. 2018, ApJS, 234, 34

Paxton, B., Smolec, R., Schwab, J., et al. 2019, ApJS, 243, 10

Pedersen, M. G., Aerts, C., Pápics, P. I., & Rogers, T. M. 2018, A&A, 614, A128

Raskin, G., van Winckel, H., Hensberge, H., et al. 2011, A&A, 526, A69

Richard, O., Michaud, G., & Richer, J. 2001, ApJ, 558, 377

Ricker, G. R., Winn, J. N., Vanderspek, R., et al. 2015, Journal of Astronomical Telescopes, Instruments, and Systems, 1, 014003

Rogers, T. M., & McElwaine, J. N. 2017, ApJL, 848, L1

Saio, H., Kurtz, D. W., Takata, M., et al. 2015, MNRAS, 447, 3264

Salaris, M., & Cassisi, S. 2017, Royal Society Open Science, 4, 170192

Schmid, V. S., & Aerts, C. 2016, A&A, 592, A116

Seaton, M. J. 2005, MNRAS, 362, L1

Stanton, L. G., & Murillo, M. S. 2016, PhRvE, 93, 043203

Szewczuk, W., & Daszyńska-Daszkiewicz, J. 2018, MNRAS, 478, 2243

Takada-Hidai, M., Kurtz, D. W., Shibahashi, H., et al. 2017, MNRAS, 470, 4908

Théado, S., Alecian, G., LeBlanc, F., & Vauclair, S. 2012, A&A, 546, A100

Théado, S., Vauclair, S., Alecian, G., & LeBlanc, F. 2009, ApJ, 704, 1262

Thoul, A. A., Bahcall, J. N., & Loeb, A. 1994, ApJ, 421, 828

Tkachenko, A. 2015, A&A, 581, A129

Townsend, R. H. D., Goldstein, J., & Zweibel, E. G. 2018, MNRAS, 475, 879

Townsend, R. H. D., & Teitler, S. A. 2013, MNRAS, 435, 3406

Turcotte, S., Richer, J., & Michaud, G. 1998, ApJ, 504, 559

Van Reeth, T., Tkachenko, A., & Aerts, C. 2016, A&A, 593, A120

Van Reeth, T., Tkachenko, A., Aerts, C., et al. 2015, ApJS, 218, 27

Van Reeth, T., Mombarg, J. S. G., Mathis, S., et al. 2018, A&A, 618, A24

Verma, K., Raodeo, K., Basu, S., et al. 2019, MNRAS, 483, 4678

Viallet, M., Meakin, C., Prat, V., & Arnett, D. 2015, A&A, 580, A61